Thermoelectric Transport in Nanoscale Materials

Joshua P. Small

Advisor: Philip Kim

Submitted in partial fulfillment of the
requirements for the degree
of Doctor of Philosophy
in the Graduate School of Arts and Sciences

COLUMBIA UNIVERSITY

2006

Abstract

Measurements of thermoelectric transport coefficients yield important information regarding fundamental properties of a system in addition to the information supplied from the electronic transport measurements. In this thesis we report gate dependent and temperature dependent conductance (G) and thermoelectric power (TEP) measurements made in three different basic nanomaterials: single-walled nanotubes (SWNTs), multi-walled nanotubes (MWNTs), and silicon nanowires (SiNWs).

There are two means of generating a thermoelectric voltage: carrier diffusion and phonon drag. Gate dependent measurements of metallic SWNTs verified the use of the mesoscopic Mott formula, the equation governing diffusive thermoelectric voltage, used to relate TEP with the conductance. We find phonon drag negligible in graphene based systems. In the semi-conducting SWNT we observed high valued and variable TEP. In addition, the TEP behaves according to a simple Schottky barrier (SB) controlled transport model where transport takes place by quantum mechanical tunneling through the barrier, or thermal activation over it, depending on the value of the gate electric field. We also observe saw-tooth oscillations of the TEP in weakly contacted SWNTs at temperatures below the charging energy, indicative of Coulomb blockade transport. Importantly, we made quantitative measurements of the TEP oscillation amplitude, agreeing well with theory.

In the MWNT, the Mott formula describes well the TEP within a framework of multiple parallel channels. We observe TEP weighting in this parallel system. In conjunction with conductance measurements, by probing the TEP in MWNTs we are able to extract the number of shells participating in electrical transport. These results agree well with figures obtained independently in controlled breakdown experiments, and the temperature dependent results may prove useful for investigation of the intershell interaction energy.

We also investigate TEP in the SiNW, where TEP response appears similar to that of the semi-conducting SWNT, but with subtle differences. In the SiNW,

both SB and bulk controlled transport contribute to the overall TEP, and must be considered within a series transport model, weighted appropriately by their length. These measurements give us insight into the SiNW transport properties.

Contents

List of Figures iii

Acknowledgments vi

1 Thermoelectric Transport 1

1.1 Introduction . . . 1

1.2 Thermoelectricity . . . 2

1.2.1 Seebeck Effect . . . 2

1.2.2 Peltier Effect . . . 3

1.2.3 Thompson Effect . . . 4

1.3 Onsager Relation . . . 4

1.4 Mott Formula . . . 6

1.5 Thermoelectric Figure of Merit . . . 9

1.6 Thermoelectricity at the Nanoscale . . . 11

2 Electronic Properties of Carbon Nanotubes 14

2.1 Introduction . . . 14

2.2 Electronic Properties of Graphene . . . 14

2.3 Carbon Nanotube Band Structure . . . 16

2.4 Ballistic Conduction in Carbon Nanotubes . . . 18

2.5 CNT Field Effect Transistors . . . 21

3 Thermoelectric transport in Single-walled Carbon Nanotubes 25

3.1 Motivation . . . 25

3.2 Device Fabrication . . . 27

3.3 Measurement Techniques . . . 28

3.3.1 ΔT Calibration . . . 28

3.3.2 DC TEP . . . 30

3.3.3 AC Double Lock-in . . . 31

3.4 Metallic SWNT Results . . . 33

3.5 Semi-conducting SWNT Results 36

4 Single-walled Carbon Nanotube as a Quantum Dot 42

4.1 Single-electron Tunneling 42

4.2 Single-walled Nanotube Quantum Dot Devices 47

4.3 Thermoelectric Power in the Coulomb Blockade Regime 49

4.4 Results 52

5 Thermoelectric Transport in Multiwalled Carbon Nanotubes 55

5.1 Electronic Transport in MWNTs 55

5.2 Results 59

6 Thermoelectric Transport in Silicon Nanowires 66

6.1 Electronic Transport in SiNWs 66

6.2 Device Fabrication 68

6.3 Results 71

7 Conclusions 78

Bibliography 79

A Appendix A - SWNT growth 84

B Appendix B - CNT Nanogap Fabrication 84

List of Figures

1.1 Seebeck Effect 2
1.2 Peltier Effect 3
1.3 Thompson Effect 4
1.4 Transport in a thermoelectric material 10
2.1 (a) Real space and (b) reciprocal space structure of graphene (reproduced from [1]) 15
2.2 (a) 2d band dispersion of graphene (b) Contour plot of 2d graphene band structure 16
2.3 An unrolled carbon nanotube (after [1]) 16
2.4 (a) Metallic NT and (b) semi-conducting NT 17
2.5 (a) Metallic NT and (b) semi-conducting NT 18
2.6 Ballistic transport 19
2.7 Schottky barrier controlled transport 23
3.1 AFM image of a SWNT "mat" sample 26
3.2 Single-walled carbon nanotube TEP device 27
3.3 Calibration measurement 29
3.4 Typical temperature and resistance changes for $P = 1\mu$W applied power 30
3.5 Measuring the DC TEP 30
3.6 DC TEP at specific V_g 31
3.7 Double lock-in technique: AC TEP and conductance 32
3.8 Qualitative verification of Mott formula 34
3.9 Measured TEP (solid) and calculation from Mott formula (dashed) . 36
3.10 Measured conductance and TEP of a s-SWNT device 37
3.11 Schottky barrier controlled transport 38
3.12 Ambipolar G and TEP behavior 40
3.13 Ambipolar G and TEP as a function of Temperature 40
3.14 Peak TEP in an ambipolar SWNT FET 41

4.1 Tunneling through a quantum dot 43
4.2 Schematic for transport through a weakly coupled quantum dot . . . 44
4.3 Energy of quantum dot as a function of effective total charge 45
4.4 SET Stability diagram 46
4.5 Coulomb blockade diamonds 47
4.6 Periodic conductance peaks in a SWNT (reproduced from [2]) 48
4.7 Predicted sawtooth oscillations of the TEP 51
4.8 Measured G (dashed) and TEV oscillations (solid) in a 2DEG quantum dot (reproduced from [3]) 51
4.9 Measured Sawtooth oscillations of the TEP in the SWNT 52
4.10 Onset of Coulomb blockade in a SWNT 53
4.11 Amplitude of TEP oscillations as a function of T 54
5.1 MWNT SPM conductance measurements (reproduced from [4]) . . . 56
5.2 Aharonov-Bohm in MWNT (reproduced from [5]) 57
5.3 Non-local IV measurements (reproduced from [6]) 57
5.4 Controlled breakdown in MWNTs (reproduced from [7] (a) and [8] (b)) 58
5.5 SEM image of a typical MWNT device 59
5.6 m-MWNT (a) and s-MWNT (b) at high and low temperatures 60
5.7 $G(V_g)$ (a) and $S(V_g)$ for a m-MWNT 62
5.8 Measured (solid) and calculated (dashed) TEP for a m-MWNT (left) and s-MWNT (right) 63
5.9 $\alpha(T)$ in a m-MWNT (cross) and s-MWNT (circle) 64
5.10 Effective number of shells in m-MWNT (cross) and s-MWNT (circle) 65
6.1 d=10nm SiNW growth direction (reprodeced from [9]) 69
6.2 SiNW's distributed on predefined alignment markers 70
6.3 Conductance of a typical SiNW device before and after rapid thermal annealing 70
6.4 $G(T)$ vs V_g for a typical SiNW device 72
6.5 $S(T)$ vs V_g for a typical SiNW device 72

6.6 DC (bottom) and AC (top) measured S vs V_g for additional SiNW devices 73
6.7 on-state SiNW TEP as a function of Temperature 74
6.8 Schottky barriers and bulk Silicon in series 74

Acknowledgments

I first thank my advisor, Philip Kim, whose dedication to his research and to his students is unbounded. He is the hardest working man I know, and also one of the most kind. I feel genuinely lucky to have been a student in his lab. Every student who works in the Kim group is proud to say that he is a member.

I am also proud to have worked with Yuanbo Zhang, Barbaros Oezyilmaz, and Mike Purewal, who are not just lab mates, but have become lifelong friends. I have many fond memories not only of working in the lab with you all, but also of the time we spent eating out, playing chess, and traveling around New York City.

Finally, I could not have done this without my family. To Mom, Dad, Jessica, and Grandma, you have all been so supportive of me. I love you all. To my wife, Wonsun, thank you for taking care of me while I was writing. I love you, and am looking forward to our wonderful future together. And to my newest family, Jinho and Uhmuhnim. You both welcomed me into your lives and have been so giving. I am honored to be a member of your family.

Thank you all.

1 Thermoelectric Transport

1.1 Introduction

The broad topic of thermoelectricity describes the direct relationship between heat and electrical energy. From a fundamental point of view, the study of thermoelectric effects can help elucidate the electronic structure and the basic scattering processes in a system. Aside from their fundamental interest, thermoelectric phenomena also underlie many practical applications. Production of a thermoelectric voltage across dissimilar metals enables us a unique method of measuring the temperature. One can create electronic cooling devices by exploiting the Peltier effect. For these reasons, scientists search for and work to develop good thermoelectric materials. Nanoscale materials, with their reduced geometries, offer an enormous variety of new and interesting materials to study.

In attempting to understand transport properties of a system, one normally applies external force to the material and measures the system's response. In the linear response regime, by applying a potential gradient,$\vec{E}$, one can measure the electrical current, $\vec{J}$, that flows and calculate the conductance, σ, governing electron transport in the system. By applying a temperature gradient,∇T, one can measure the heat which flows and calculate the thermal conductance, κ, from the relation $\vec{Q} = \kappa\vec{\nabla}T$, governing thermal transport in the system. We can combine these equations of transport into a matrix equation relating generalized forces and their corresponding currents.

$$\begin{pmatrix} \vec{J} \\ \vec{Q} \end{pmatrix} = \begin{pmatrix} L_{11} & L_{12} \\ L_{21} & L_{22} \end{pmatrix} \begin{pmatrix} \nabla V \\ -\nabla T \end{pmatrix} \tag{1.1}$$

Here V is the electric potential and L_{ij} are constants independent of V and T. We immediately recognize L_{11} as the electrical conductance, σ and L_{22} as the thermal conductance, κ. The non-zero off-diagonal components, on the other hand, serve to mix heat and charge, and give rise to three interrelated thermoelectric phenomena: the Seebeck, Peltier, and Thompson effects.

In this chapter we discuss the manifestation of these thermoelectric effects (section 1.2), Onsager's theorem and the relationship between the off-diagonal components (section 1.3), the Mott formula (section 1.4), the thermoelectric figure of merit, ZT (section 1.5), and finally we discuss thermoelectricity at the nanoscale (section 1.6).

1.2 Thermoelectricity

Here we examine the fundamental thermoelectric effects. Some of these effects are large and relatively easy to measure in bulk (Seebeck), while others present considerably more experimental challenge (Thompson). Later, it will be shown that the measurement of any one of these effects is sufficient to explain the thermoelectric properties of a material.

1.2.1 Seebeck Effect

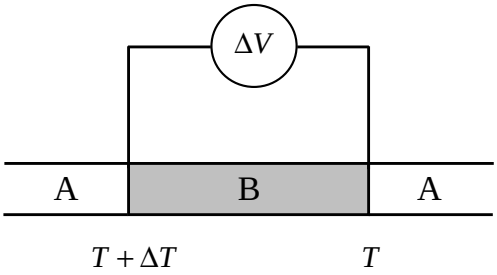

Figure 1.1: Seebeck Effect

We begin by creating a temperature difference, ΔT, across some material, B, in an electrically open circuit. A voltage difference, ΔV, develops in response to the temperature gradient. The ratio of the voltage to the applied temperature difference is called the thermoelectric power (TEP), or equivalently, the Seebeck coefficient, S.

$$S = -\frac{\Delta V}{\Delta T} \tag{1.2}$$

The origin of the voltage which develops across the sample can be understood in the following crude, but simple explanation. The application of a temperature gradient causes the charge carriers at each end of the sample to have different energies. It can be argued that on average the higher energy electrons will also have a higher velocity, and will tend to diffuse toward the colder end of the sample. Thus, initially an electric current, $\vec{I}$, begins to flow. However, since we experimentally restrict current from flowing, charge collects until the electric field is large enough that $\vec{I}$ becomes zero.

One additional note is that the experimental setup in figure 1.1 will not yield the absolute thermopower S_B, but rather the difference in thermopower between the two materials $S_B - S_A$. The reason for this is simply that the metal electrodes (material A) used to contact material B experience the same temperature gradient, but biased in reverse. In order to measure the absolute thermopower of a material, one must either know the absolute TEP of the contact electrodes in advance, or use superconducting electrodes for which $S = 0$.

Solving the transport equation (1.1) with $\vec{I} = 0$, we can identify $L_{12} = \sigma S$. The diffusive TEP is calculated by evaluating L_{12} in the Boltzmann formalism, which will be discussed in section 1.4.

1.2.2 Peltier Effect

We now allow current to flow in our system, but hold the temperature of each end fixed at the same temperature, T.

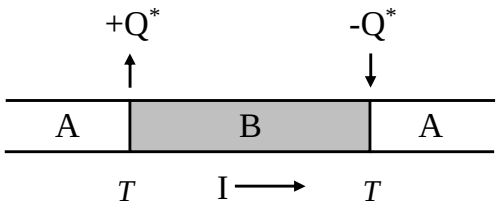

Figure 1.2: Peltier Effect

We again refer to equation 1.1, and find that along with the electrical current,

$\vec{I}$, a thermal current $\vec{Q} = \frac{L_{21}}{L_{11}}\nabla V$ also flows. Because the transport coefficients for materials A and B are different, heat is generated at one junction and absorbed at the other in order to preserve continuity of $\vec{Q}$. The transport quantity L_{21}/L_{11} is called the Peltier coefficient, Π.

Since an amount of heat energy Q^* is absorbed at one of the junctions, the Peltier effect can be used to transfer heat from one junction to another, which can be utilized for thermoelectric refrigeration. However, in typical conductng systems Joule heating dominates, making efficient Peltier cooling a difficult task.

1.2.3 Thompson Effect

Besides Peltier cooling there is an additional means of generating reversible heat in a medium. I briefly describe the Thompson effect, by which a temperature gradient is applied to a current carrying conductor.

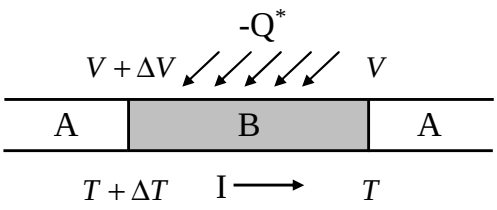

Figure 1.3: Thompson Effect

In this case a reversible heat is generated in the bulk of the conductor. The Thompson coefficient μ describes the rate of heat generation per unit current flow per unit temperature gradient. Measurements of μ are extremely difficult owing to the presence of Joule heating.

1.3 Onsager Relation

This section describes the relationship between the various thermoelectric coefficients, and follows Ziman [10]. We begin by rewriting the transport equation (1.1) in a completely general form

$$J_i = \sum_j L_{ij} X_j \tag{1.3}$$

where J_i are generalized currents and X_i are the corresponding generalized forces. The Onsager relation (equation 1.4) states that the matrix of transport coefficients is symmetric

$$L_{ij} = L_{ji} \tag{1.4}$$

and follows from thermodynamic principles [11]. The argument given involves investigation of the rate of entropy production under non-equilibrium conditions:

$$\dot{S} = \sum_i J_i X_i = \sum_{ij} L_{ij} X_i X_j \tag{1.5}$$

In order to relate the thermoelectric transport coefficients we must first determine the generalized forces X_1 and X_2. We begin by identifying J_1 as the electrical current $\vec{J}$, and J_2 as the thermal current $\vec{Q}$, and calculating contribution to entropy production due to each.

We start with the entropy generated by the electrical current. Thermodynamics states that this should simply be Q_{JH}/T where Q_{JH} is the heat produced in the sample due to Joule heating. Thus, $\dot{S} = \vec{J} \cdot \vec{E}/T$ and the generalized force X_1 is given by $\nabla V/T$.

In order to calculate entropy produced by flow of a thermal current $\vec{Q}$, we first write down an expression for the entropy current $\vec{S} = \vec{Q}/T$. The equation of continuity relates its divergence to the rate of change of entropy in the region

$$\dot{\vec{S}} = \nabla \cdot \vec{S} = \nabla \cdot \frac{\vec{Q}}{T} = \vec{Q} \cdot \nabla \frac{1}{T} \tag{1.6}$$

where the last equality follows from constancy of $\vec{Q}$. We now have all the information necessary to reconstruct equation 1.1 in terms of our generalized forces and currents:

$$\begin{pmatrix} J_1 \\ J_2 \end{pmatrix} = \begin{pmatrix} L_{11}T & -L_{12}T^2 \\ L_{21}T & -L_{22}T^2 \end{pmatrix} \begin{pmatrix} X_1 \\ X_2 \end{pmatrix} \tag{1.7}$$

Using Onsager's relation we identify $L_{21} = -TL_{12}$. This allows us to relate all the transport coefficients described in section 1.2. We now explicitly write the working form of the Onsager relations for thermoelectricity as follows:

$$\Pi = ST \qquad\qquad \mu = T\frac{dS}{dT} \tag{1.8}$$

1.4 Mott Formula

To investigate thermoelectric phenomena experimentally, one can in principle measure any one of the thermoelectric transport coefficients: S, Π, or μ. Reversible heat is challenging to detect due to Joule competition, so the measured coefficient is generally the thermopower, S. On the other hand, conceptually it is more straightforward to compute Π and then obtain the thermopower through the Onsager relations. Although it is based on a microscopic description of a conducting system, rather than the thermodynamic argument, there is another relation between S and σ, called the Mott formula. We sketch the outline of the derivation using the Boltzmann equation, following Ziman [10] and Moss [12]. The original derivation is due to Cutler and Mott [13].

$$\Pi = \frac{\vec{Q}}{\vec{J}} \tag{1.9}$$

The Peltier coefficient relates the amount of thermal current to the amount of electrical current flowing through a material when an external electric field is applied (equation 1.9). Physically, this corresponds to the amount of heat transported per unit charge. Using the Onsager relation, we identify the thermopower as the amount of entropy transported per unit charge. To caclulate the Peltier coefficient it is necessary to evaluate the expressions below, for $\vec{J}$ and $\vec{Q}$

$$\vec{J} = \int e\vec{v}_{\vec{k}} f_{\vec{k}}\, \mathrm{d}\vec{k} \qquad\qquad \vec{Q} = \int E_{\vec{k}}\vec{v}_{\vec{k}} f_{\vec{k}}\, \mathrm{d}\vec{k} \tag{1.10}$$

where $f_{\vec{k}}(\vec{r})$ is the distribution function for states $\vec{k}$ around the neighborhood of $\vec{r}$. The problem is now equivalent to solving for the distribution function under the

application of a temperature gradient and an electric field. This is typically done by solving the Boltzmann equation, which is derived from examining the rate of change of the distribution function due to diffusion, applied external fields, and scattering, in steady state [10]. Below (equation 1.11) the Boltzmann equation is written in its linearized form

$$-\vec{v}_{\vec{k}} \cdot \frac{\partial f^0_{\vec{k}}}{\partial T} \nabla T - \vec{v}_{\vec{k}} \cdot e \frac{\partial f^0_{\vec{k}}}{\partial E_{\vec{k}}} \vec{E} = \int \{(f_{\vec{k}} - f^0_{\vec{k}}) - (f_{\vec{k'}} - f^0_{\vec{k'}})\} T^{\vec{k'}}_{\vec{k}} \, \mathrm{d}\vec{k'} \tag{1.11}$$

where $T^{\vec{k'}}_{\vec{k}}$ is intrinsic transition rate between states $\vec{k}$ and $\vec{k'}$, and $f^0_{\vec{k}}$ is the equilibrium distribution. Using this result it is possible to write down an expression for the electric current in equation 2.3 under conditions of a spherical energy surface.

$$\vec{J} = -\frac{e^2}{4\pi^3} \int \int \tau(k) \vec{v}_{\vec{k}} \vec{v}_{\vec{k}} \frac{\partial f^0_{\vec{k}}}{\partial E_{\vec{k}}} \, \mathrm{d}S \frac{\mathrm{d}E}{|\partial E / \partial \vec{k}|} \cdot \vec{E} \tag{1.12}$$

where dE and dS are the change in energy and change in the constant-energy 2D Fermi surface, respectively. A relationship between the microscopic transition rate, $T^{\vec{k'}}_{\vec{k}}$, and inverse scattering time, $1/\tau(k)$, has been implicitly made under isotropic conditions [10]. The expression is simplified when we identify the density of states as $N(E) = (2\pi^3 |\partial E / \partial \vec{k}|)^{-1}$. The electric current can be rewritten in a simple form [13]:

$$\vec{J} = -e^2 \int \frac{1}{3} \tau(E) v^2 (\frac{\partial f}{\partial E}) N(E) \mathrm{d}E \tag{1.13}$$

Similarly, one can write down an expression for the thermal current:

$$\vec{Q} = -ke \int \frac{1}{3} \tau(E) v^2 \frac{E - E_F}{k_B T} (\frac{\partial f}{\partial E}) N(E) \mathrm{d}E \tag{1.14}$$

where k_B is Boltzmann's constant, and E_F is the Fermi energy. Because $|\frac{\partial f}{\partial E}|$ rapidly approaches zero away from the Fermi energy, we can evaluate the integrals in 1.14 and 1.13 by Taylor expanding $N(E)$ about the Fermi energy [12]:

$$N(E) = N(E_F) + \frac{\mathrm{d}N}{\mathrm{d}E}|_{E_F} (E - E_F) + \frac{1}{2} \frac{\mathrm{d}^2 N}{\mathrm{d}E^2}\Big|_{E_F} (E - E_F)^2 + \cdots \tag{1.15}$$

Only the anti-symmetric terms from the expansion contribute to the integral, and the thermopower has the form:

$$S = -\frac{\pi^2}{3}\frac{k_B}{e}\frac{kT}{N(E)}\frac{\mathrm{d}N}{\mathrm{d}E}\Big|_{E_F} \tag{1.16}$$

Multiplying on top and bottom by the small energy window, kT, around E_F, we can change from density of states to electron density, $N(E) \rightarrow n(E)$. Now, by identifying the DC conductivity as $\sigma = ne^2\tau/m$ we rewrite the expression for thermopower in the following form:

$$S = -\frac{\pi^2}{3}\frac{k_B^2 T}{e}\frac{\mathrm{d}\ln\sigma}{\mathrm{d}E}\Big|_{E_F} \tag{1.17}$$

where e is the sign of the positron charge.

Equation 1.17 is the Mott formula. We will often compare our measured TEP to that predicted by the Mott formula, so here we mention some of its notable properties.

First, the formula contains a term $k_B/e \sim 80\mu\mathrm{V}/K$, which can be considered the natural unit of thermopower. We can expect measured values of TEP to be roughly on the order of this natural value.

Second, the derivative of the log of conductivity in the expression means that the TEP is a very sensitive probe of the electronic structure of the material. It is for this reason that we can expect a large, tunable TEP in the semi-conducting nanotube, as the conductance in the subthreshold regime can be steep as a function of energy.

Third, there is a linear temperature dependence. Metallic and metallic-like materials whose conductivity do not have an appreciable temperature dependence are expected to exhibit this linear temperature dependance.

Fourth, we mention how scattering information is encoded into the Mott formula. The Mott formula is a function of the conductivity, whose expression contains the scattering time, τ. If τ is a function of the energy, $\tau(E) \propto E^p$, then measurements of the thermopower can illuminate the nature of the scattering mechanism in the

material [12]. For instance, hard-sphere scattering has an exponent $p = -1/2$, but Rutherford scattering from a Coulombic potential has $p = -2$.

It is necessary to mention that the diffusive Mott term is not the only mechanism for thermopower generation. There exists another physical means by which a thermoelectric voltage can be set up. With application of a temperature gradient, phonons are preferentially directed from the hot end of the sample towards the cold. These phonons can scatter off of electrons and impart momentum to them, motivating an electric current to flow. Of course, a thermoelectric voltage must be generated to prevent this charge flow. This is another source of thermoelectric power in a medium. The so called phonon drag term of TEP can be roughly written as $S_{drag} \sim \alpha_{e-ph} c \tau_{pp} / \tau_{ep}$, where τ_{pp} is the phonon-phonon scattering time, τ_{ep} is the electron-phonon scattering time, c is the lattice specific heat, and α_{e-ph} is a constant proportional to the electron-phonon interaction strength. The electron-phonon interaction in graphite is extremely weak [14], and we do not expect measurable contributions to the carbon nanotube TEP from phonon drag.

In this thesis we are going to discuss the validity of the Mott formula in various 1-dimensional systems. Good agreement with the Mott formula in the metallic SWNT verifies its application at the mesoscopic scale [15]. Moreover, this agreement confirms that the contribution of TEP due to phonon drag is negligible in carbon nanotubes. Experiments with semi-conducting SWNTs reveal a high and variable TEP, and support the Schottky barrier controlled transport picture. Finally, the Mott formula's application to MWNTs allow us to probe the density of states as a function of the temperature. These results are presented in section 3.

1.5 Thermoelectric Figure of Merit

Thermoelectric cooling and power conversion are attractive practical applications of the thermoelectric effects described in section 1.2. The strength of these effects and suitability for application are determined by their thermoelectric figure of merit, ZT [16, 17]:

$$ZT = \frac{S^2\sigma}{\kappa} \tag{1.18}$$

This dimensionless parameter is a function of the usual transport coefficients. A quick derivation serves to illustrate their placement in the definition of ZT.

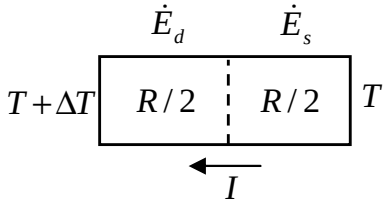

Figure 1.4: Transport in a thermoelectric material

To calculate the rate of energy change in the drain side of the device pictured in figure 1.4, it is necessary to sum all contributions to the heat flow. $\dot{E}_d = STI - I^2R/2 - K\Delta T$ governs rate of energy change in the drain due to thermoelectric cooling, Joule heating, and thermal backflow. To maximize ΔT, $\dot{E}_d$ should be zero. We solve $\mathrm{d}\dot{E}_d/\mathrm{d}I = 0$ for the current $I_0 = ST/R$ which maximizes ΔT. The maximum achievable temperature difference is then given by [18]:

$$\Delta T_0 = \frac{S^2T^2}{2RK} = \frac{ZT^2}{2} \tag{1.19}$$

where we identify the thermoelectric figure of merit as $ZT = S^2T\sigma/\kappa$. The fractional change in temperature, $\Delta T/T$, is then directly proportional to ZT.

The thermopower, S, describes how much heat is carried per unit charge, and enters in the numerator. Higher TEP yields higher TE efficiency. The electrical conductivity, σ, determines how much energy is lost due to Joule heating. The larger σ, the less Joule heat produced and the more efficient the material. κ governs thermal transport in the system. A temperature gradient is built up by the electronic transport of heat, but thermal energy will tend to leak back across the conductor. The more thermally resistive the sample, the better its candidacy for thermoelectric application.

Bulk thermoelectric figures of merit at $T = 300K$ hovered around $ZT \leq 1$ throughout the 1990's. To make a major contribution to electronic cooling would require that $ZT \sim 1.4$, and to significantly impact air-conditioning ZT should approach a value $ZT > 2.5$ [19]. Production of high-ZT materials is challenging because of the strong interrelationship between the transport coefficients. The Wiedermann-Franz law frustrates attempts to increase ZT by increasing the electrical conductance, because the thermal conductance is raised by a corresponding amount. Thus, much of the century saw little improvement in the TE figures of merit of bulk materials.

More recently, however, advances in control over material growth (such as MBE) enabled the production of new and exotic materials. The ability to tailor thin films sparked interest in enhancing ZT in two distinct ways. One method seeks to exploit quantum confinement effects in quantum dot superlattices [18]. The other method enhances ZT by use of a phonon-blocking/electron transmitting superlatice which reduces thermal conductance by creating acoustic mismatch in the lattice [17]. These superlattice structures produced record breaking values of TE figures of merit. Experiments on p-type Vi_2Te_3/Sb_2Te_3 superlattice reported $ZT = 2.4$ at room temperature [17].

The strong promise of these 2-dimensional (2d) superlattice materials makes the extension to 1-dimensional (1d) nanomaterials, such as silicon nanowires (SiNWs), automatic [16, 20]. Additionally, in 1d materials the increased boundary scattering of phonons and quantum confinement of phonons further reduces the thermal conductance, making them attractive as potential TE devices.

1.6 Thermoelectricity at the Nanoscale

Here we briefly discuss some of the fundamental reasons why transport at the mesoscopic scale is different from that in bulk. Many reasons underlie the unique transport mechanisms in nanostructures, but among the most important are: energy

quantization due to confinement, the electron-electron interaction, and phase coherence. These will be discussed one by one as to their impact on thermoelectric phenomena.

As material size is reduced, one of the most obvious fundamental differences to the bulk properties is the increasing separation, or quantization, of its energy levels. The discrete occupation of these energy states has a major impact on the material's electrical and thermal transport properties. As will be discussed in chapter 2, it leads to quantization of the electrical conductance in units of $g_0^{el} = \frac{2e^2}{h}$, experimentally observed in 1988 [21, 22]. Quantization of 1d thermal conductance in units of $g_0^{th} = \pi^2 k_B^2 T/3h$ was also observed in a suspended bridge structure [23]. It is an interesting question to ask how the thermoelectric figure of merit, ZT, scales with device size. For n occupied electronic modes, and p occupied phonon modes, a simple calculation yields the figure of merit.

$$ZT = \frac{S^2\sigma}{\kappa}T \rightarrow 80.8\frac{n}{p+n}[S(\mathrm{mV/K})]^2 \tag{1.20}$$

In a SWNT it is possible to occupy only the lowest 4 phonon modes ($p = 4$) and 2 electrical modes ($n = 2$). A $ZT > 3$ would be achievable at modest values of the TEP ($S \sim 300\mu$V/K).

As size and dimensionality of a system is reduced, the amount of phase space the charges have to distribute themselves drastically decreases. As the charges are confined to a smaller space, their electrostatic interaction with one another becomes comparatively large. If the system is only weakly coupled to a charge reservoir, the electron-electron interaction leads to Coulomb blockade (CB). At low temperatures, transport through the structure is blocked except for certain values of the chemical potential. Conductance and TEP behave in a drastically different way from their bulk behavior. Thermoelectric transport in the Coulomb blockade region is discussed in chapter 4.

Finally, when the device scale becomes smaller than the phase coherent length, phase coherent transport is observed. In samples of few or no defects, charges can

move ballistically through the sample. Ballistic conduction is discussed in chapter 2. When transport is phase coherence, the Mott formula is applied in its mesoscopic form:

$$S = -\frac{2\pi^2}{3}\frac{k_B^2 T e}{h}\frac{\mathrm{d}\ln T_r(E)}{\mathrm{d}E}\Big|_{E_F} \tag{1.21}$$

where $T_r(E)$ is the energy dependent transmission coefficient. In a 1d system the conductance can be replaced with transmission probability through the Landauer formula, $(2e^2/h)T_r(E)$ [24]. The derivation of this mesoscopic Mott formula was carried out by Sivan and Imry [25], and experimentally observed in quantum point contacts formed in a 2d electron gas [3]. It will be interesting to test the mesoscopic scale Mott formula in 1d nanoscale materials such as carbon nanotubes and semiconducting nanowires.

2 Electronic Properties of Carbon Nanotubes

2.1 Introduction

Carbon nanotubes have firmly established themselves as highly interesting systems both for the study of fundamental physics and for their strong potential for use in electronic applications. Since their discovery in 1991 they have been the subject of numerous experimental and theoretical studies. By now many of their electrical properties are quite well known, and here we will briefly discuss some of the main properties relative to this thesis in the following text.

First, we discuss the electronic properties of graphene (section 2.2), the band structure of carbon nanotubes (section 2.3), ballistic conduction in carbon nanotubes (section 2.4), and carbon nanotube field effect transistors (section 2.5).

2.2 Electronic Properties of Graphene

The carbon nanotube is essentially a rolled up sheet of graphene. As such it is necessary to start by studying graphene's electronic properties. Graphene is a two-dimensional array of carbon atoms arranged in a hexagonal structure. Figure 2.1 diagrams the graphene structure in real space (a) and reciprocal space (b). The four $n = 2$ shell electrons hybridize in the sp^2 configuration: per carbon atom, three in-plane σ bonds form the strong hexagonal lattice and one covalent, out-of-plane π bond ultimately determines the electron transport properties of the system.

The band structure is calculated within the tight binding model. Two carbon atoms per unit cell allow us to compose Bloch functions out of the atomic orbitals of the two carbon atoms. By only considering nearest-neighbor interactions it is possible to derive the π-π^* band structure.

Within the tight-binding scheme, solving the secular equation leads to the following equation for the band dispersion relation, obtained as a function of the 2d wave vectors, (k_x, k_y):

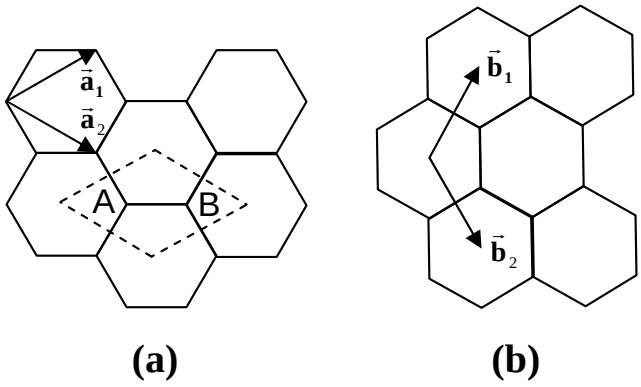

Figure 2.1: (a) Real space and (b) reciprocal space structure of graphene (reproduced from [1])

$$E(k_x, k_y) = \pm t\sqrt{1 + 4\cos\left(\frac{\sqrt{3}k_x a}{2}\right)\cos\left(\frac{k_y a}{2}\right) + 4\cos^2\left(\frac{k_y a}{2}\right)} \qquad (2.1)$$

Here the nearest neighbor hopping integral is $t = 2.5$eV and the length of the lattice vector is $a = 0.246$nm.

We now plot the band structure for a single sheet of graphene. Figure 2.2a shows energy on the z-axis as a function of k_x and k_y. Figure 2.2b gives a contour plot of the energy of the π^*-band. Because there are two π electrons per unit cell, these electrons exactly fill up the $E < 0$ π-band. One can also calculate the band structure for the σ-bands of graphene, but these bands are located further away from $E_F = 0$. Thus, the low energy transport properties are completely determined by the π-π^* bands.

The low energy band structure of graphene is in fact quite unique. The energy bands are linear around the charge neutral Fermi level. In contrast to a Fermi surface, at the Fermi energy there exist two inequivalent Fermi points. Bands cross at two inequivalent points $\vec{K}$ and $\vec{K'}$ as consequence of the two-atom unit cell. In this respect, graphene is a zero-gap semiconductor. Depending on the direction of transport graphene can behave as a metal or as a semiconductor.

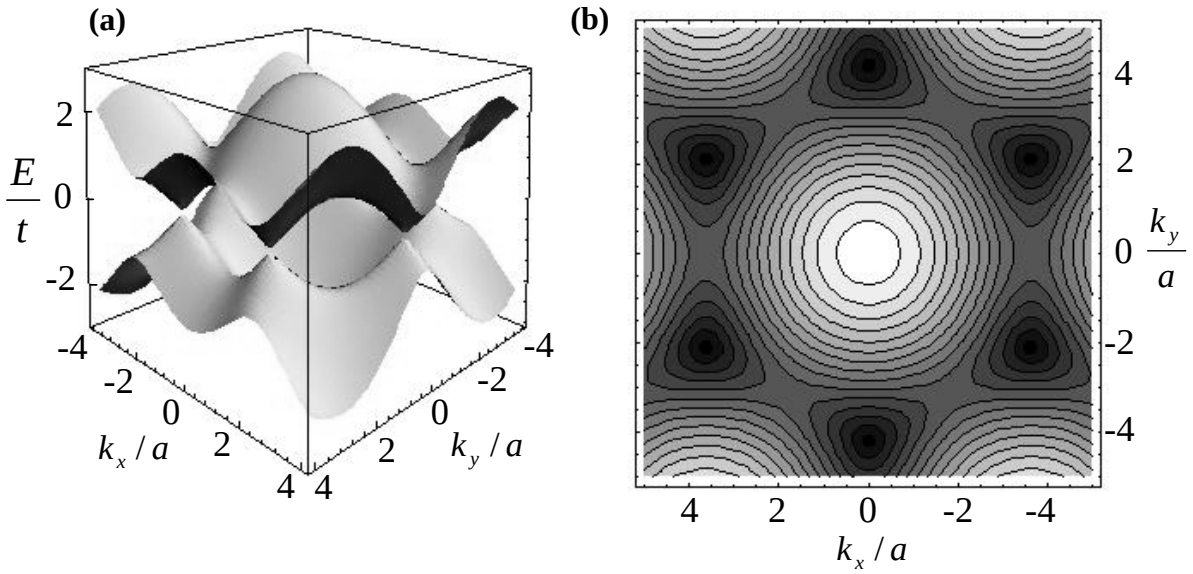

Figure 2.2: (a) 2d band dispersion of graphene (b) Contour plot of 2d graphene band structure

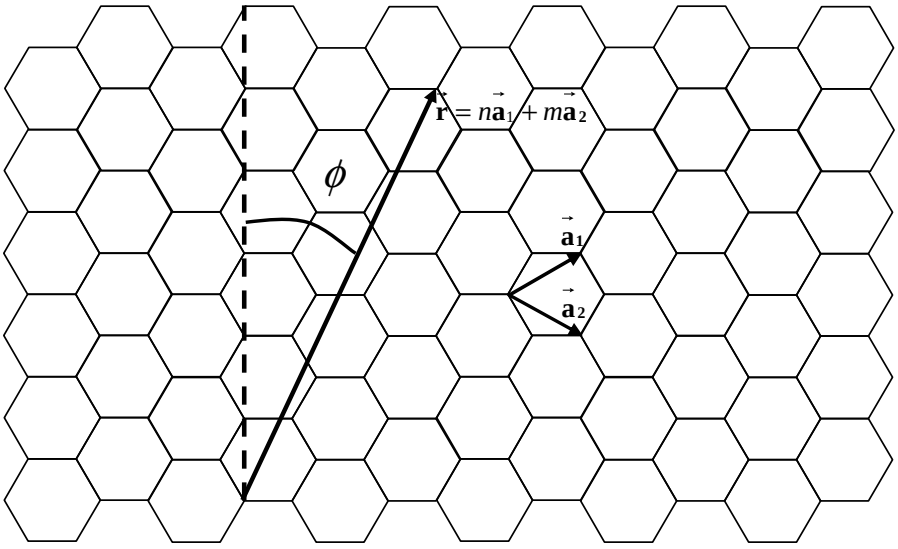

Figure 2.3: An unrolled carbon nanotube (after [1])

2.3 Carbon Nanotube Band Structure

Since a carbon nanotube is essentially a rolled up cylinder of graphene, in the lowest approximation the band structure of a CNT can be obtained from that of graphene by imposing periodic boundary conditions. Figure 2.3 again shows the honeycomb

structure of graphene. The way in which the graphene sheet is rolled is defined by its chiral vector, $\vec{r} = n\vec{a_1} + m\vec{a_2}$, where n and m are integers and $\vec{a_1}$ and $\vec{a_2}$ are the two lattice vectors defined in figure 2.1. By connecting the cites defining the vector $\vec{r}$ we create an (n, m) carbon nanotube. There are two distinct structural classes of carbon nanotubes: achiral and chiral. The former has a mirror image identical to the original, where the latter does not. Of the achiral nanotubes there are again two classes: (n, n) armchair and $(n, 0)$ zig-zag, so named for the shape of their cross section.

Single-walled nanotubes (SWNTs) typically have diameters of $d \sim 1.5$nm. We expect the transport properties of SWNTs to be similar to that of graphene, but with modifications due to quantum mechanical confinement in the circumferential direction. Periodic boundary conditions lead to quantization of the perpendicular component of momentum and act to restrict values of $\vec{k}$ to a subset of states. The allowed $\vec{k}$ vectors determine whether the resulting nanotube will be metallic or semi-conducting. If the allowed set of $\vec{k}$ vectors include $\vec{K}$ or $\vec{K'}$ the resulting nanotube is metallic, otherwise it is semi-conducting (Figure 2.4).

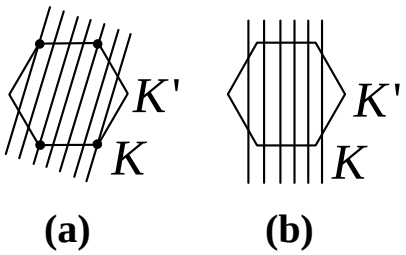

Figure 2.4: (a) Metallic NT and (b) semi-conducting NT

Restricting the $\vec{k}$ values to this subset of states effectively slices up the 2-dimensional graphene band structure into 1d subbands (figure 2.5). The subbands are separated by an energy $\Delta E = \hbar v_F/d$, the lowest lying obviously being the slice closest to the $\vec{K}$ point, where $v_F \sim 8 \times 10^5$m/s is the Fermi velocity of graphene.

The band structure information is contained in the (n, m) indices describing the chirality of the nanotube. Using the graphene band structure, one can calculate

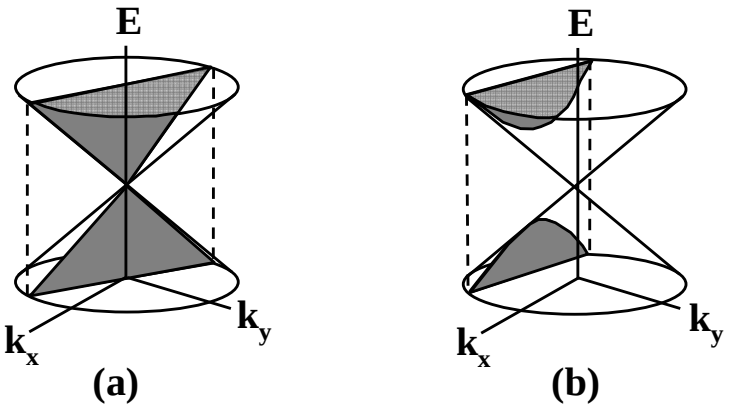

Figure 2.5: (a) Metallic NT and (b) semi-conducting NT

the 1d band structure for any (n, m) nanotube. A simple rules emerges: if $n - m$ is a multiple of 3 then the nanotube is metallic, otherwise it is semi-conducting. Furthermore, in semi-conducting tubes, the bandgap is related to the NT diameter:

$$E_g = \frac{a_{C-C}|t|}{d} \tag{2.2}$$

where $a_{C-C} = 1.42\mathring{A}$ is the carbon-carbon bond length, $d = a\sqrt{n^2 + m^2 + nm}$ is the nanotube diameter, a is the lattice constant in figure 2.1a, and $|t|$ is the orbital overlap. Taking $|t| = 2.5$eV, the gap goes roughly as $E_g = 0.8eV/d$[nm]. In fact, STM experiments explicitly demonstrated the connection between NT structure and their electronic properties [26, 27].

One can probe more deeply into these fundamental electrical and mechanical properties of carbon nanotubes, and the interested reader is directed to Saito [1], an excellent reference on the subject.

2.4 Ballistic Conduction in Carbon Nanotubes

High quality carbon nanotubes exhibit electron transport with a mean free paths up to 0.5μm at room temperature and are expected to be ballistic conductors [28]. This section briefly reviews the Landauer-Büttiker formalism for ballistic transport and its connection with carbon nanotubes. I follow the presentation given by Datta

[24] and Heinzel [29].

A material's conductance is expected to scale linearly with its width and inversely to its length, as $G = w\sigma/L$. This law is intuitive, yet breaks down at small scales. When device length becomes smaller than some fundamental length scale of the system (i.e, mean free path,l_{mfp}, and phase coherent length, l_ϕ one enters the mesoscopic regime. As our length becomes smaller than the mean free path of the system $L \ll l_{mfp}$ instead of diverging, the conductance approaches a constant value G_c. Below we explain the origin of this finite resistance in a ballistic channel.

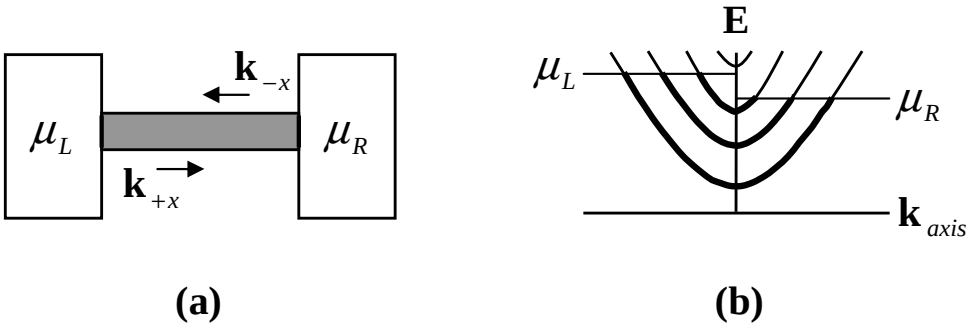

Figure 2.6: Ballistic transport

Assume two charge reservoirs are separated by a narrow, ballistic conductor (figure 2.6a). The small size of the conductor quantizes $k_\perp$ leading to the 1d subbands shown in figure 2.6b. The reservoirs on the left and right are held at electrochemical potentials μ_L and μ_R, respectively. The contacts are taken to be infinitely conducting and reflectionless. If a $+\vec{k}$ $(-\vec{k})$ state enters the conductor it empties into the right (left) contact without reflection. Thus, right (left) moving states can only be supplied by the left (right) contact.

If $\mu_L = \mu_R$ then the number of $+\vec{k}$ and $-\vec{k}$ states are equal and no current flows, as expected. By biasing the left and right reservoirs with a potential $V_{sd} = (\mu_L - \mu_R)/e$, we increase the number of right movers with respect to left-movers and a current begins to flow.

We first consider the simple case of single subband occupation and reflectionless contacts, where the transmission coefficient, T_r is equal to 1. $T_r < 1$ transmission

and multiple subbands will be reintroduced at the end of the calculation. The current is written as:

$$I = \int \Big(N_{+k}(E) f_L(E)(1 - f_R(E)) v_{+k}(E) - N_{-k}(E) f_R(E)(1 - f_L(E)) v_{-k}(E) \Big) \mathrm{d}E \tag{2.3}$$

where $N_{\pm k}(E)$ is the 1-d density of states of the right and left moving charges, and $f_{L,R}(E)$ are the Fermi functions in each electrode. The one dimensional density of states for left and right moving electrons is given by

$$N(E) = \frac{1}{2\pi\hbar}\sqrt{\frac{2m}{E}} \tag{2.4}$$

where m is the electron mass, and we have already accounted for the spin-degeneracy.

The electron velocity is given by $v(E) = \sqrt{\frac{2E}{m}}$ and thus explicitly cancels the contribution from the 1-d density of states. We are left with

$$I = \frac{e}{\pi\hbar} \int \big(f_L(E) - f_R(E) \big) \, \mathrm{d}E \tag{2.5}$$

We now recast the Landauer equation in a convenient form. The drain is biased with a voltage V_d with respect to the source, at ground. We also let the transmission probability drop below unity and also allow it to depend on energy.

$$I = \frac{e}{\pi\hbar} \int \big(f(E) - f(E + eV_d) \big) T_r(E) \, \mathrm{d}E \tag{2.6}$$

The introduction of multiple subbands does not add further difficulty as long as the number of subbands, M, is constant throughout the bias window. If we now let the transmission probability go to $T_r = 1$, and examine the expression at low temperatures where $f(E)$ is roughly a step function, then the integral yields $(\mu_L - \mu_R) \times M$. We arrive at a simple formula:

$$G = \frac{2e^2}{h} M \tag{2.7}$$

This is a surprising result which states that in ballistic conductors the conductance should be quantized in units of $g_0 = 2e^2/h$. Indeed, the first experimental

measurements of quantized conductance made on quantum point contacts verified equation 2.7 [21, 22].

If transport in the carbon nanotube is truly ballistic one should expect to measure a conductance $G_0 = 2 \times 2e^2/h$, the factor of 2 coming from the $\vec{K}$, $\vec{K}'$ lattice degeneracy. Indeed, conductance quantization has been observed in the carbon nanotube [30, 31]. These transport experiments used source-drain contacts on the order of $L = 1\mu$m. To realize ballistic transport the device length must be $L < l_{mfp}$, suggesting that at low temperatures ($T < 4$K)in the CNT $l_{mfp} > 1\mu$m and that carbon nanotubes are high quality conductors.

2.5 CNT Field Effect Transistors

Silicon technology is rapidly reaching its fundamental size limit. To further reduce the transistor size it is necessary to investigate molecular scale devices for switching applications. First reports of the creation of a carbon nanotube field-effect transistor (NT-FET) naturally sparked a huge interest in such devices [32, 33]. In conventional metal-oxide-semiconductor FETs (MOSFET), switching is controlled by pinch-off in the depletion layer [34]. Attempts to explain the NT-FET mechanism as similar to that of the MOSFET fail to work, however, and the Schottky barrier controlled FET picture quickly became the dominant theory [35, 36].

At a metal-semiconductor interface an energy barrier is formed in order to align the Fermi levels. This energy barrier is called a Schottky barrier (SB), and ignoring effects due to Fermi level pinning it is determined by the work function of the metal and ionization potential of the semi-conductor in 1d [37]. For most materials, the FET action is still governed by pinch-off in the bulk as described above, but still limited somewhat by the SB formed at the interface [34]. In the case of carbon nanotubes, however, the Schottky barrier plays a dominating role, whereby the transistor action is completely governed by SB modulation and the NT bulk behaves as a ballistic conductor [36, 38, 39].

Even before the emergence of a fully developed theory, experiments hinted at the

strong influence of Schottky barriers in NT-FET devices. Reports of ambipolar NT-FETs attributed the behavior to strong modulation of the barrier by the electrostatic gate field [35]. In another experiment, reversible conversion between p and n-type behavior was realized by annealing devices in an O_2 environment and in vacuum [40]. It was suggested that O_2 at the contact plays a strong role in determination of the SB height, a very different mechanism from that of doping. Finally, scanning gate microscopy, a means of locally gating mesoscopic scale devices, demonstrated strong current modulation only when the local gate was near the NT-metal interface [41].

Further experiments improved upon NT device characteristics and exhibited high performance behavior [42], by using Pd as a contact metal [43] or high capacitance electrolytic gating [44]. Large diameter SWNT's exhibited ambipolar behavior, though n-type conduction was significantly lower than that of p-type [45, 46, 47].

Qualitatively, NT-FET behavior can be understood as follows. Consider a metal-NT-metal interface where the metal work function and NT bandgap is such that the Fermi level falls exactly in the center of E_g (figure 2.7). A Schottky barrier is formed at the interface and no current flows through the NT. When negative gate bias is applied, the NT bands shift upward. Thermal activation of holes over the SB begin to turn the device on. Larger negative gate bias thins the SB even more, so that tunneling is possible. In this state the NT-FET is considered completely turned on. This simple model assumes that once charge carriers enter the NT, conduction is ballistic, and they do not scatter in the bulk.

This is a simplified version of the now accepted model put forth in late 2002 [36, 38, 48]. Actual theoretical models calculate $G(V_g, V_{sd})$ via the Landauer formula (equation 2.6) in conjunction with $T_r(E)$ determined by WKB methods, using a self-consistent electrostatic potential from the solution of Poisson's equation.

Results of the above calculations quantitatively confirm many experimental observations. First, submicron scale NT-FET characteristics exhibit no length dependence for devices $L < 1\mu$m [36]. The bulk nanotube merely acts as a ballistic channel

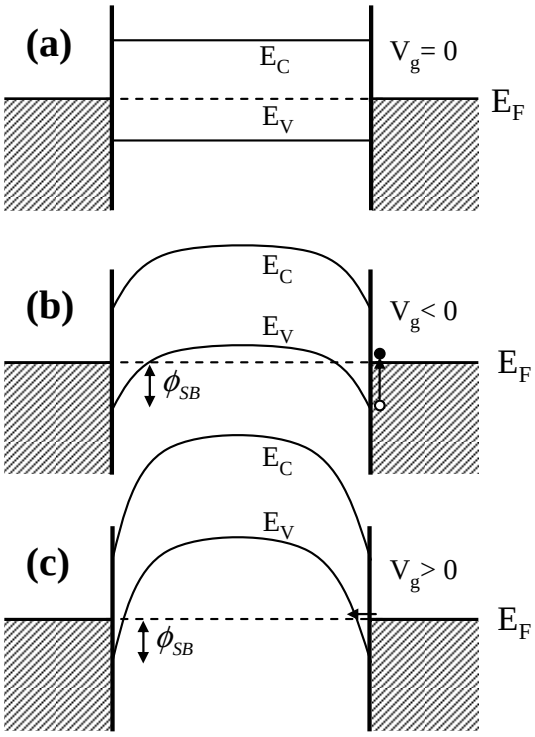

Figure 2.7: Schottky barrier controlled transport

between two Schottky barriers. Second, the role of O_2 is to change the metal electrode work function [38], altering device characteristics appropriately. Finally, the inverse subthreshold slope, $S_{th} = dV_{gs}/d(\log I_d)$, saturates at a constant value below $T \sim 200K$ and shows significant dependence on gate electrode coupling. None of these findings can be explained by typical MOSFET operation, but become clear in the SB controlled FET picture [36].

Further work led to improvement in device characteristics by adjusting NT-FET geometry and NT-FET behavior now rivals that of standard Si technology [49, 39, 50, 43]. Work continues to more deeply understand the nature of semiconducting nanotube behavior. Recent studies seek to explain the critical role played by electrode metal choice [51], understand current saturation in the s-SWNT [52], and explore behavior of long, diffusive NT-FET's [53].

In section 3.5 we discuss thermoelectric transport in the s-SWNT where we discover a potential application of the s-SWNT as we find a large electric field

modulated TEP.

3 Thermoelectric transport in Single-walled Carbon Nanotubes

In this section we report our measurement of thermoelectric power (TEP) of an individual carbon nanotube [15, 54]. We modulate both the conductance and TEP by gate electric field, and notice a strong relationship between the two. The measured TEP agrees well with that predicted by the 1d mesoscopic scale Mott formula, providing additional evidence that transport in the single-walled nanotube (SWNT) is coherent at the 1μm length scale, even at room temperature. Absence of a phonon drag term in the measured TEP suggests that electron-phonon coupling is weak in the CNT, as expected. We also investigate the TEP in the semi-conducting nanotube, and measure large values which are extremely sensitive to the Fermi level. At temperatures below the single electron charging energy we measure large oscillations in TEP, which are discussed in the following chapter.

In this chapter we first discuss motivation (3.1), followed by device fabrication (3.2), electrical measurement technique (3.3), results in metallic SWNTs (3.4), and finally results in semi-conducting SWNTs (3.5).

3.1 Motivation

A mesoscopic scale measurement of TEP in SWNTs is desirable for many reasons. For one, the TEP is a transport quantity which is highly sensitive to the change in electronic structure at the Fermi energy. We can use the TEP to probe the electronic properties of the SWNT, including scattering mechanisms inside the tube. Secondly, as previously mentioned nanoscale structures are promising thermoelectric materials. The possibility of high-valued, tunable thermopower in the semi-conducting nanotube make CNTs attractive for potential thermoelectric applications, as discussed in section 3.5.

There have been numerous experiments designed to measure TEP of SWNT bulk samples, often called "mat" samples. The first of such experiments reported

$S \sim 50\mu V/K$ at room temperature [55]. At first glance this is an unexpected result. A charge neutral nanotube with a linear band structure should have a diffusive TEP of roughly zero [55]. Further study of TEP in mat samples demonstrated their extreme sensitivity to environment [56, 57, 58]. Exposure to O_2 and its subsequent removal demonstrated sign change of the TEP. The TEP was also found to be sensitive to the adsorption of hydrocarbons on CNT films.

Temperature dependent measurements of the TEP can in principle yield information about transport and scattering mechanisms in the tubes. Yet, typical mat samples naturally contain many SWNTs in addition to numerous tube-tube junctions (figure 3.1).

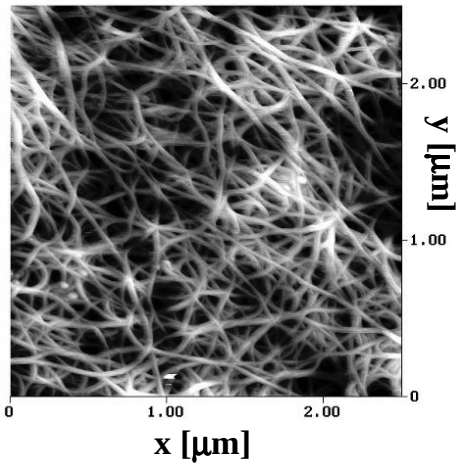

Figure 3.1: AFM image of a SWNT "mat" sample

A disadvantage to measurements made on such mat samples is that they cannot avoid including extrinsic effects arising from tube-tube junctions. These junctions arguably contribute the majority of the resistance to the sample. Another downside is that mat samples contain an ensemble of nanotubes of varying chirality. Thus, the measurement produces TEP over an ensemble average of CNTs. For these reasons it is difficult to measure the intrinsic TEP of the CNT using mat samples.

By fabricating a device designed to measure TEP in an individual SWNT, we can overcome many of these issues and measure TEP for a particular chirality of

nanotube. Another advantage of isolating a single tube, is that we can now change a well-defined Fermi energy inside the SWNT using a back gate. This will allow us to investigate the energy dependence of the mesoscopic scale Mott formula.

3.2 Device Fabrication

We begin by growing SWNTs on a Si-SiO_2 substrate by chemical vapor deposition. Details of the growth can be found in appendix A. We grow on a substrate of relatively large Si oxide thickness, t_{ox} = 500nm. The SWNTs are located with respect to pre-fabricated alignment markers by scanning electron microscope (SEM). Next, thin (t=100nm wide) Cr/Au metal electrodes are fabricated on top of the SWNT by electron beam lithography. We make electrical contact to the SWNT with source and drain electrodes (each in a 4-probe geometry). In addition we fabricate a thin microheater nearby, but not in electrical contact with the SWNT. The metals are deposited by thermal evaporation and have thicknesses of roughly Cr=5nm and Au=30nm. We then liftoff the PMMA in acetone overnight. An SEM image of the device is shown in figure 3.2.

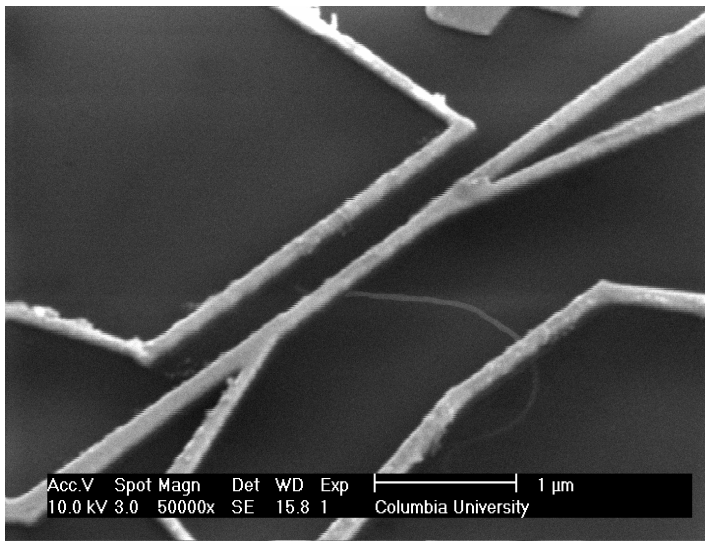

Figure 3.2: Single-walled carbon nanotube TEP device

Through Joule heating we build up a temperature gradient across the substrate

by applying a current I_h to the heater line. The source and drain serve a dual purpose, as they not only measure current and voltage in the nanotube, but can also function as microthermometers, since R_s and R_d change with the temperature (see figure 3.4). The four probe configuration allows us to measure $R_s(I_h)$ and $R_d(I_h)$, the resistance of the electrodes as a function of applied heater current, without inclusion of the contact resistance. This enables us to determine the temperature difference between the electrodes.

Before discussing the measurement it is important to address length scales of some of the relevant device parameters. Compared to the majority of devices designed to study transport in SWNTs, our SWNT TEP device has a thick oxide. Thinner oxides are normally desired because they facilitate better gate coupling (higher C_g) to the nanotube. However, the thermal conductivity of bulk Si is approximately 50 times that of SiO_2. Any heat produced would quickly flow through the bulk Si in a thin oxide device, and not allow the creation of a stable temperature gradient. The thick oxide is necessary to maintain this temperature gradient along the substrate.

Let us also address the need for exceedingly thin (100nm wide) metal contacts to the nanotube. Generally, we find that the contact resistance to the NT is higher when using thin (100nm) electrodes than when using μm-scale contacts. However, measurement of the TEP requires a precise measurement of the temperature at both the source and drain. For this reason, it is necessary to locally probe the temperature on a significantly smaller scale than the device length ($L = 1\mu$m).

3.3 Measurement Techniques

3.3.1 ΔT Calibration

A temperature gradient is set up along the SWNT upon applying a current I_h to the microheater. The following measurement yields the temperature difference across the SWNT by measuring the rise in the temperature at the source and drain, ΔT_s and ΔT_d.

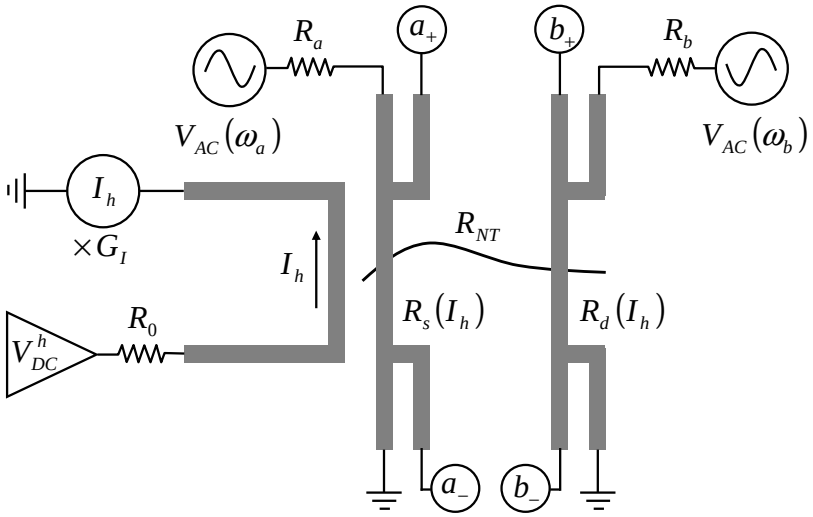

Figure 3.3: Calibration measurement

We sweep a voltage V_{DC}^h applied to the microheater in series with a resistance $R_0 = 1\text{k}\Omega$. V_{DC}^h is applied using the DAC output of a NI DAQ. Instead of directly applying V_{DC}^h to the microheater, we add a series resistor and increase the applied voltage range, enhancing the resolution. Current is read using an Ithaco 1211 current amplifier.

The source and drain resistances are measured by an SR830 lock-in amplifier. We operate the lock-ins in constant current mode by adding a series resistance $R_a = 100\text{k}\Omega \ll R_{s,d}$. An output voltage of $V_{AC} = 1\text{V}$ at $\omega_a = 23\text{Hz}$ is applied by lock-in 'a' corresponding to a $10\mu\text{A}$ excitation current. A similar signal is applied to R_d at $\omega_b = 11\text{Hz}$ by lock-in 'b'. Measuring the voltage developed across $R_{s,d}$ yields the four-probe resistance. Because $\Delta R_{s,d}(I_h)$ is very small, we internally offset the lock-in input. Lock-in settings used are sens = 10mV, $\tau = 300\text{ms}$, and we expand the output by a factor of 100.

To calculate the temperature difference, we must cross-reference curves of $R_{s,d}(I_h)$ measured at two nearby temperatures. Below, we plot $\Delta R_{s,d}(I_h)$ for a typical device near room temperature.

The change in resistance should go as $\Delta R = \alpha R_0 \Delta T$ where α is the temperature coefficient of resistance, TCR, of the metal. We find that $\Delta T \propto I_h^2$ as expected from

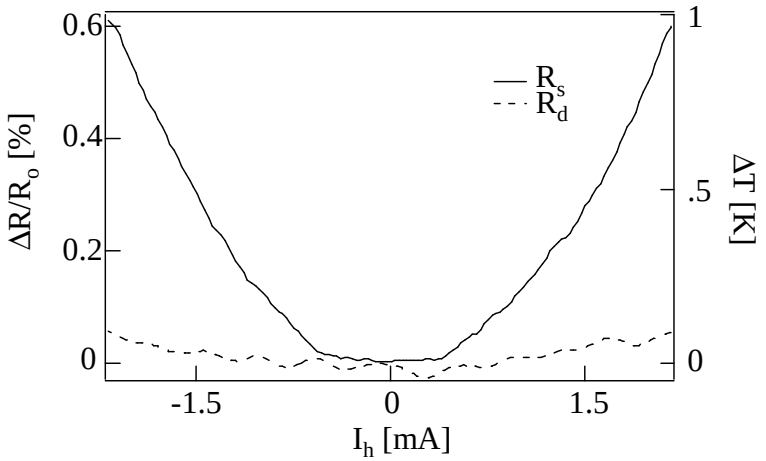

Figure 3.4: Typical temperature and resistance changes for $P = 1\mu$W applied power

a linear heat transfer model. A power $P = 1\mu$W applied to the microheater creates roughly a 1K temperature difference across the nanotube at room temperature. The power was adjusted at lower temperatures to ensure $\Delta T \ll T$ in order to stay in the linear response regime.

3.3.2 DC TEP

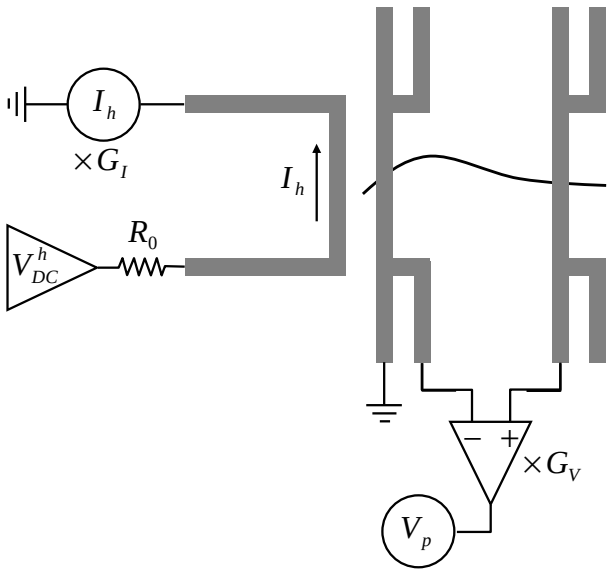

Figure 3.5: Measuring the DC TEP

Figure 3.5 gives the schematic for DC TEP measurement. We set up a temperature gradient just as in the calibration measurement: by sweeping a DC voltage, V_{DC}^{h}, applied to the microheater. A differential voltage preamplifier (SR560 or Ithaco 1201) measures the thermoelectric voltage developed across the SWNT, $\Delta V_p(I_h)$. For fixed values of V_g we observe that $\Delta V_p \propto I_h^2 \propto \Delta T$. We obtain the TEP of the SWNT by the relation $S = \Delta V_p/\Delta T$. A typical plot shown in diagram 3.6.

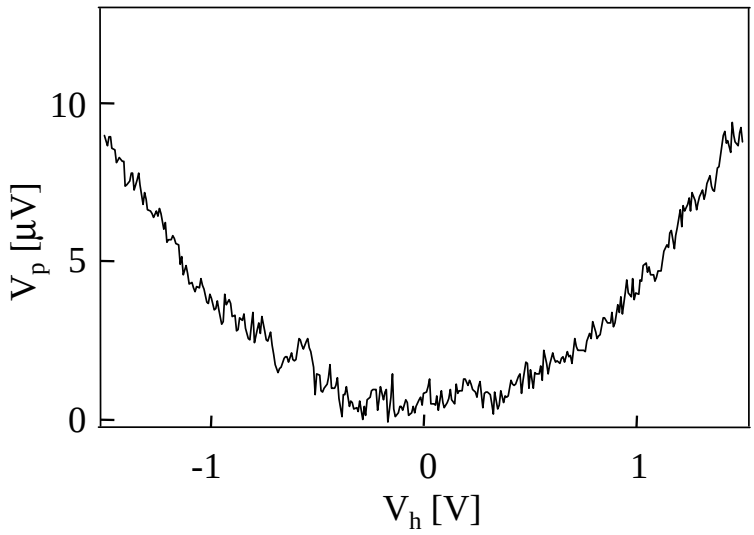

Figure 3.6: DC TEP at specific V_g

Fitting $\Delta V_p(I_h)$ gives us one data point for S at a particular gate voltage. We then increment V_g and another sweep is performed. In this way, we can measure $S(V_g)$.

3.3.3 AC Double Lock-in

While the previous method for measuring TEP is very robust, it also has its disadvantages. For one, it is quite time consuming. If the device exhibits significant TEP modulation as a function of the energy, one will necessarily need to take many data points. Each data point at a particular V_g requires a slow sweep of I_h. A second disadvantage exists due to hysteresis in the device. In the analysis we must compare

$S(V_g)$ and $G(V_g)$. The DC TEP and DC conductance cannot easily be measured simultaneously, and so the comparison is more difficult when the curves are obtained from different gate voltage sweeps.

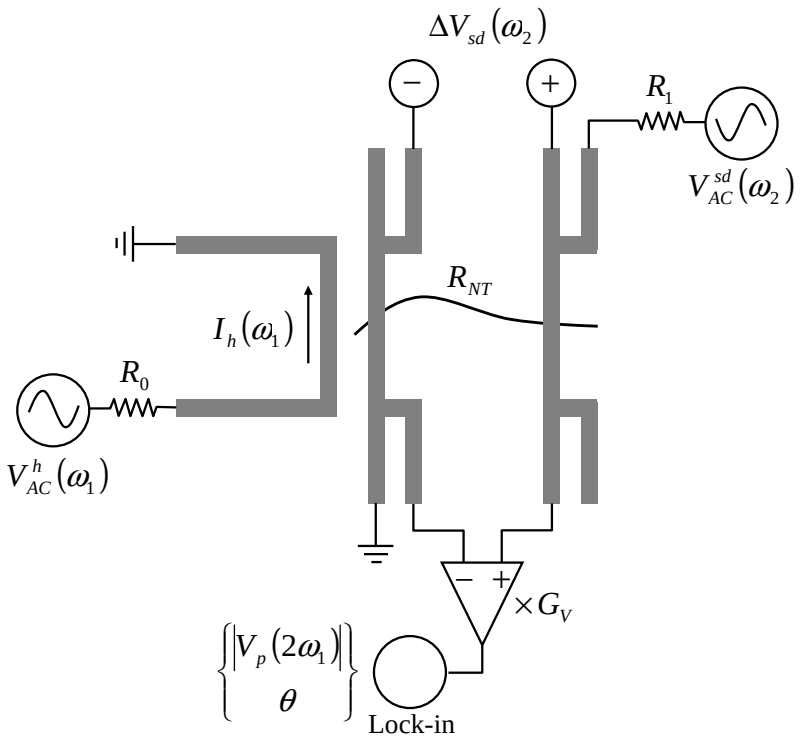

Figure 3.7: Double lock-in technique: AC TEP and conductance

The AC double lock-in technique simultaneously measures both G and TEP, and requires significantly less time. Figure 3.7 diagrams the measurement schematic. To measure the TEP across the nanotube we apply a time varying signal, $V_{AC}^h(t) = V_0^h \sin\omega_1 t$, to the microheater. A thermoelectric voltage develops according to equation 3.1

$$\Delta V_{te}(t) = S\Delta T = S\beta V_0^h \sin\omega_1 t^2 = \frac{S\Delta T_0}{2}(1 - \cos 2\omega_1 t) \tag{3.1}$$

where β is the proportionality constant relating applied temperature difference and heater current $\Delta T_0 = \beta(V_0^h)^2$, and is quantified by the calibration measurement. We feed the signal through a differential voltage amplifier (Ithaco 1201) and detect

it using the lock-in. We measure the thermopower by sensing the $2\omega_1$ signal, which is $\pi/2$ out of phase.

Simultaneously we apply a small voltage V_{AC}^{sd} to the nanotube using a second lock-in amplifier. A series resistor $R_1 \gg R_{NT}$ in parallel with the nanotube will supply a constant current along the SWNT. Conductance is calculated by measuring the voltage that develops across the nanotube, ΔV^{sd}.

Now we sweep the gate voltage and measure both signals simultaneously. Care must be taken in ensure that the two measurements do not interfere with one another. The signal frequencies must be chosen such that their harmonics are not picked up by the other lock-in amplifier. The applied TEP frequency should be slowly varying $\omega_1 \propto 1.54$Hz so that the temperature difference which develops is in phase with the applied heater voltage. For this reason the time constant τ should be quite long and the gate voltage sweep speed should be slow. Additionally, in the case of semi-conducting SWNTs the TEP is limited by the input impedance of G_V and R_1. These settings should be chosen with care.

3.4 Metallic SWNT Results

We measured the conductance and TEP of nearly ten devices as a function of gate voltage and temperatures ranging from 300K down to 1.8K. We note that our measurement cannot probe the absolute thermopower due to the nanotube, but measures its TEP with respect to the metal electrodes: $S = S_{NT} - S_{elec}$. Due to the bulk nature of the metal electrodes, S_{elec} should not vary with the gate voltage. Therefore, any modulation in the signal can be attributed solely to the SWNT.

Ideally, a metallic SWNT should have a flat conductance curve, yet all of our devices exhibit modulation in both G and TEP. There are two strong possibilities for the origin of this structure: resonant defect tunneling and small bandgap semiconductor behavior, as discussed below.

Variation in the conductance has been ascribed to resonant tunneling scattering through defects in the CNT [59, 60]. SGM experiments confirm the existence of

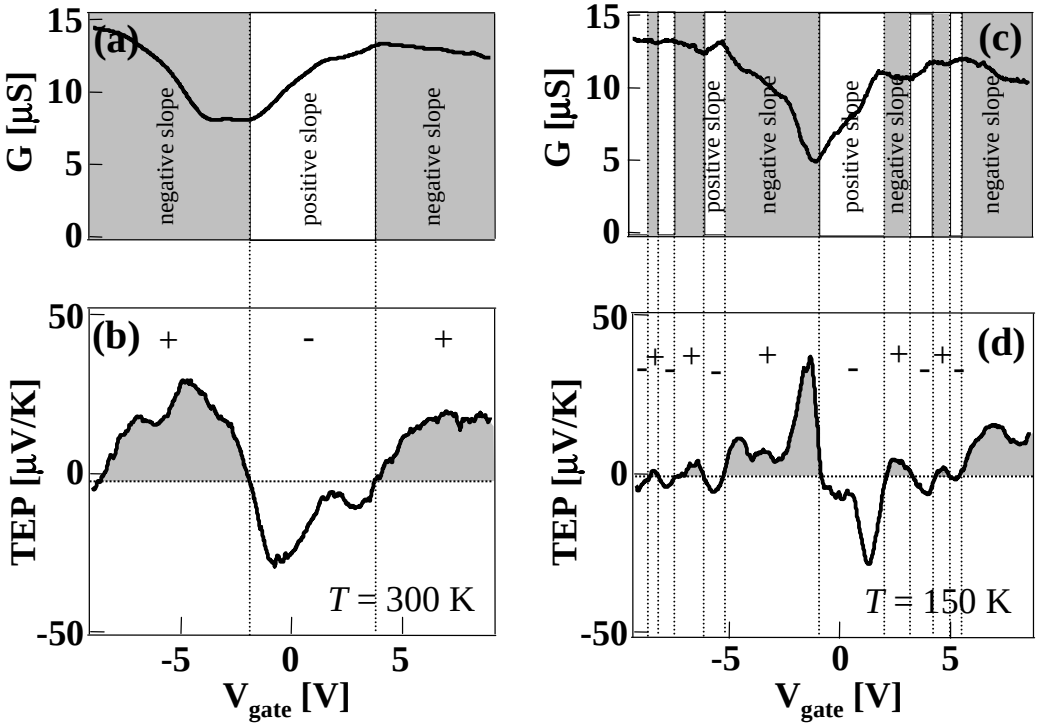

Figure 3.8: Qualitative verification of Mott formula

such defects in SWNT devices. The defects complicate the potential landscape for electrons in the CNT, and give rise to structure in the transport. This effect is stronger at lower temperatures, and thus the structure becomes more complicated as T decreases. Another possible reason for the structure is that these metallic nanotubes are in fact very-small-bandgap semi-conductors [61]. While symmetry ensures that the achiral metallic SWNT CNT **K** and **K′** bands should cross each other unaffected, it is possible that a symmetry breaking mechanism opens up a small gap at the Fermi energy. Possibly the mechanism is a curvature induced symmetry breaking, which opens up a band gap on the order of 10 to 100meV [61].

Data from a typical metallic SWNT is presented in figure 3.8. At room temperature the device exhibits a dip in the conductance (a), while the TEP twice changes sign in the same region of gate voltage (b). At lower temperature we observe more structure in the conductance (c) and more sign changes in the TEP (d). In fact, there is a correlation between these two transport quantities: the TEP changes sign at the

conductance minima and maxima. After subtracting a small offset from the TEP it is possible to relate the thermopower to the derivative of the conductance. The small offset is $\sim -4\mu$V/K at T=300K, and becomes smaller at lower temperature. We believe that this small offset corresponds to the thermopower contribution of the metal electrodes. The thermopower of bulk Au is $\sim 5\mu W/K$ at room temperature, in reasonable agreement with the value of the offset.

A quantitative correlation between S and G is made by comparing the measured TEP to that calculated from the Mott formula (equation 3.2). As previously noted, the Mott formula should still hold for 1-dimensional mesoscopic conducting channels, where the conductance is related to the electron transmission coefficient, T, by the Landauer expression $G = (2e^2/h)T_r$ [25]:

$$S = -\frac{\pi^2}{3}\frac{k_B^2 T_r}{e}\frac{d\ln T_r}{dE} \tag{3.2}$$

In order to calculate the predicted TEP using the Mott formula, we must relate the change in gate voltage, V_g, to the the change in electrochemical potential in the nanotube, ΔE_F. We can write down the relationship as

$$C_g \Delta V_g = \rho_{SWNT} \Delta E_F \tag{3.3}$$

where the density of the states in the SWNT is $\rho_{SWNT} = 8e/hv_F$. The gate capacitance is measured from Coulomb blockade analysis (discussed in chapter 4). We measure $C_g = 15$pF/m, in reasonable agreement with calculation from a simple geometrical model [33].

Figure 3.9 shows the quantitative comparison between the measured TEP and that predicted by the Mott formula. All 5 of our metallic SWNT devices qualitatively obeyed the Mott formula for all temperatures. Additionally, we were able to measure the capacitive coupling in the Coulomb blockade regime to quantitatively compare two of these devices to theory. Both of these devices exhibited excellent quantitative agreement between the Mott formula and the measured TEP, not only

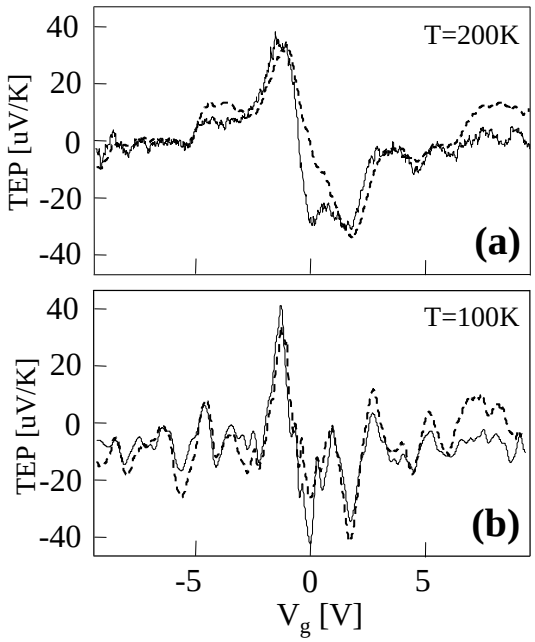

Figure 3.9: Measured TEP (solid) and calculation from Mott formula (dashed)

with the peak position, but also in the TEP height. This measurement was successful in quantitatively verifying the validity of the mesoscopic scale Mott formula. Additionally, the excellent agreement also shows that phonon drag does not contribute to the TEP in the SWNT, signifying the weak electron-phonon coupling in graphene.

3.5 Semi-conducting SWNT Results

The basic electronic behavior of semi-conducting nanotubes based on Schottky barrier controlled transport was discussed in section 2.5. In this section we measure the thermoelectric properties of the s-SWNT and seek to explain the behavior of the thermoelectric power.

Figure 3.10 shows the conductance and TEP of a typical p-type semi-conducting SWNT. Examining the upper graph of the log of the conduction versus gate voltage, one can identify three distinct regions of interest defined by the threshold voltage, V_{th}: (I) $V_g \ll V_{th}$, the on-state with high and saturated G; (II) $V_g \sim V_{th}$, the

subthreshold regime where the device begins to turn off; (III) $V_g \gg V_{th}$, the off-state with strongly suppressed G. Correspondingly, the lower graph exhibits three distinct regions of TEP behavior. In the on-state we find a large, saturated TEP value of $S \sim 120\mu$V/K at room temperature, and as the device begins to turn off the TEP peaks at $S \sim 260\mu$V/K.

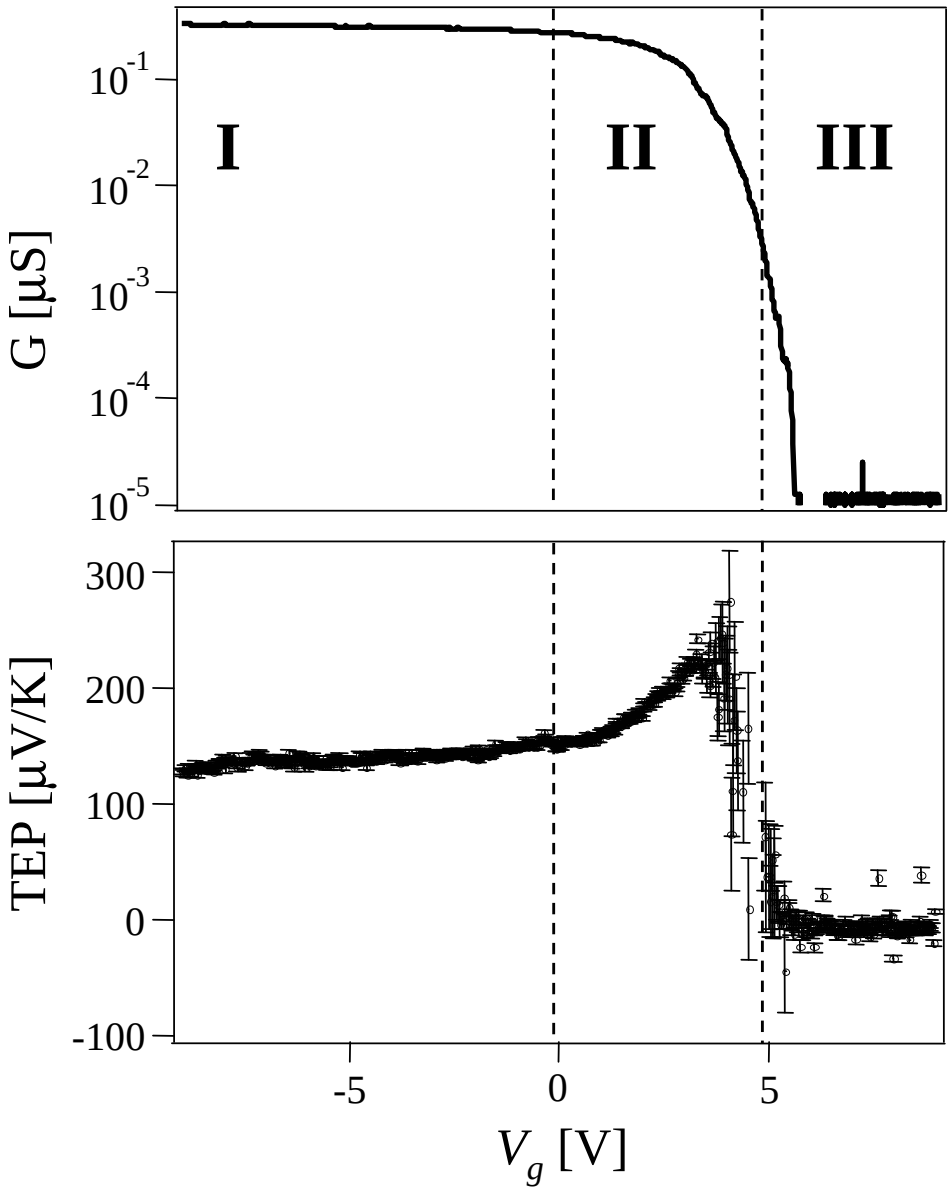

Figure 3.10: Measured conductance and TEP of a s-SWNT device

To explain TEP behavior, we use the same SB-controlled transport picture that

others have used to explain the conductance behavior in the SWNT FET [49, 50]. Figure 3.11 again diagrams the Schottky barrier in the three distinct regions of transport. In the on-state (I), the barrier is very thin and conduction proceeds by charges tunneling through. In the sub-threshold regime (II), the barrier is significantly wider, and thermal activation of charges over the barrier is the dominant mode of conduction. In region (III) the Fermi level is in the middle of the bandgap and no conduction occurs. We can compare the measured TEP values to the predictions of the Mott formula by using a simple model to describe the conductance in each of the regions.

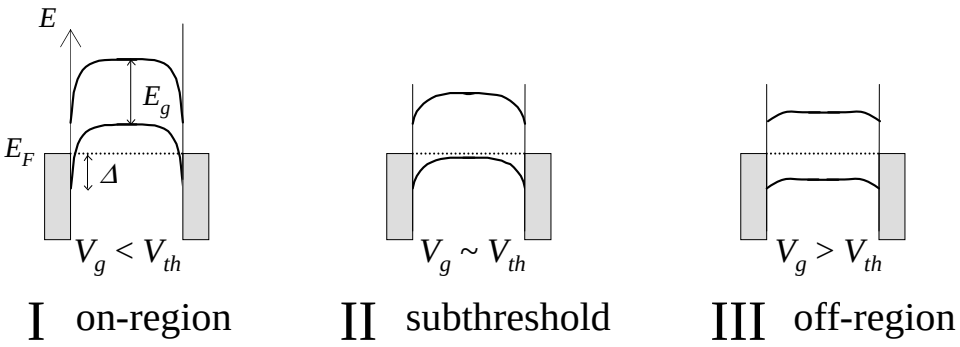

Figure 3.11: Schottky barrier controlled transport

In region (I), we model the tunneling of charges through a barrier of height Δ using the WKB approximation. In this region, the conductance is expected to behave as $G(E) \sim \frac{4e^2}{h} e^{-\gamma\sqrt{\Delta - E}}$, where γ is a constant independent of E since the SB width is saturate to $\sim t_{ox}$ in the on-state [49]. We can re-write γ in terms of the on-state conductance G_0:

$$\gamma = \ln \frac{G(0)}{4e^2/h} \tag{3.4}$$

Using the Mott formula we can now write an expression for the TEP in the on-state region as:

$$S_{sat} = \frac{\pi^2 k_B^2 T}{6e\Delta} \ln \frac{G(0)}{4e^2/h} \tag{3.5}$$

where our only free parameter is the Schottky barrier height, Δ. We can test the model by calculating Δ using the room temperature measured TEP and G values. Upon doing this, we obtain $\Delta = 160$meV, which agrees well with the observed p-type behavior in this SB SWNT FET.

In the subthreshold regime, the dominant mechanism for transport is thermionic emission over the Schottky barrier. Conductance in the thermally activated regime is expected to go as $G(E) \sim e^{-(E-\Delta)/k_B T}$. As a result, we expect to find a positive value of the TEP in the subthreshold regime of:

$$S = \frac{\pi^2 k_B}{3e} = 284\mu\text{V/K} \tag{3.6}$$

which agrees well with the observed room temperature value.

Although by far the majority of our CVD grown nanotubes were p-type, we occasionally managed to measure the TEP and conductance of a rare ambipolar SWNT FET device. From our simple model, we expect to find anti-symmetric TEP behavior in the ambipolar device. This antisymmetric behavior is apparent in figure 3.12. Note that the peak TEP is $S_{peak} \sim 280\mu$V/K for both sides of the curve.

We measured the temperature dependence of the transport coefficients in a different ambipolar device. We expected to find a temperature independent peak TEP value in the subthreshold regime. Figure 3.13 diagrams the conductance and TEP of the ambipolar device from temperatures ranging T=300K to T=100K.

The results appear to support our simple model describing the TEP in SWNT FETs. We see anti-symmetric behavior in the TEP, although the p-type transport behavior is not as clean as the n-type behavior. As we cannot easily define a peak TEP in the p-type side of this sample, we plot the n-type peak TEP versus temperature in figure 3.14. The peak fluctuates within acceptable error around the predicted value of $S = 284\mu$V/K.

In conclusion, we have demonstrated interesting high and variable TEP modulation in a SWNT FET. A simple transport model seems to support SB controlled

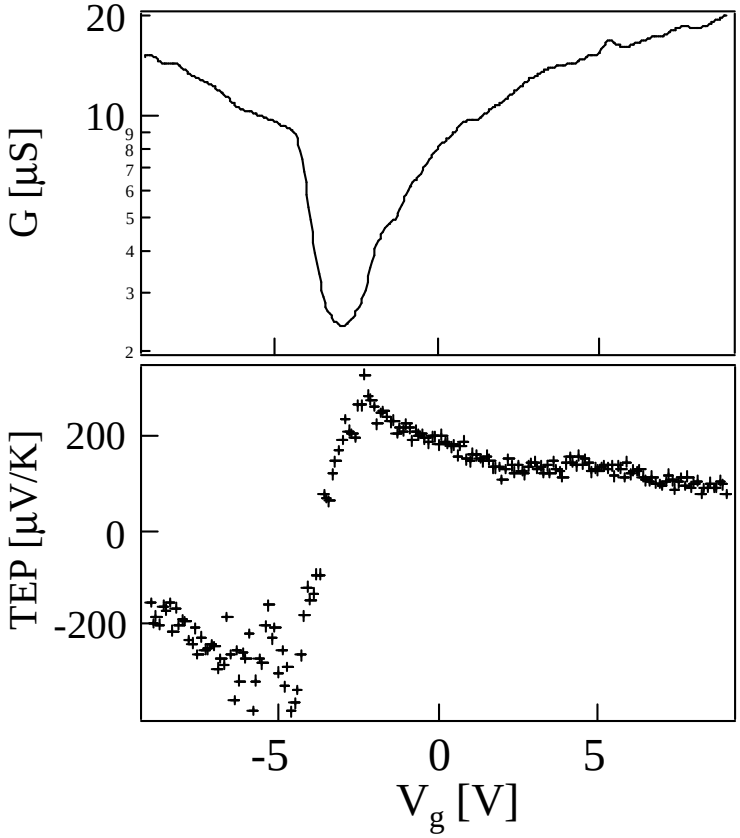

Figure 3.12: Ambipolar G and TEP behavior

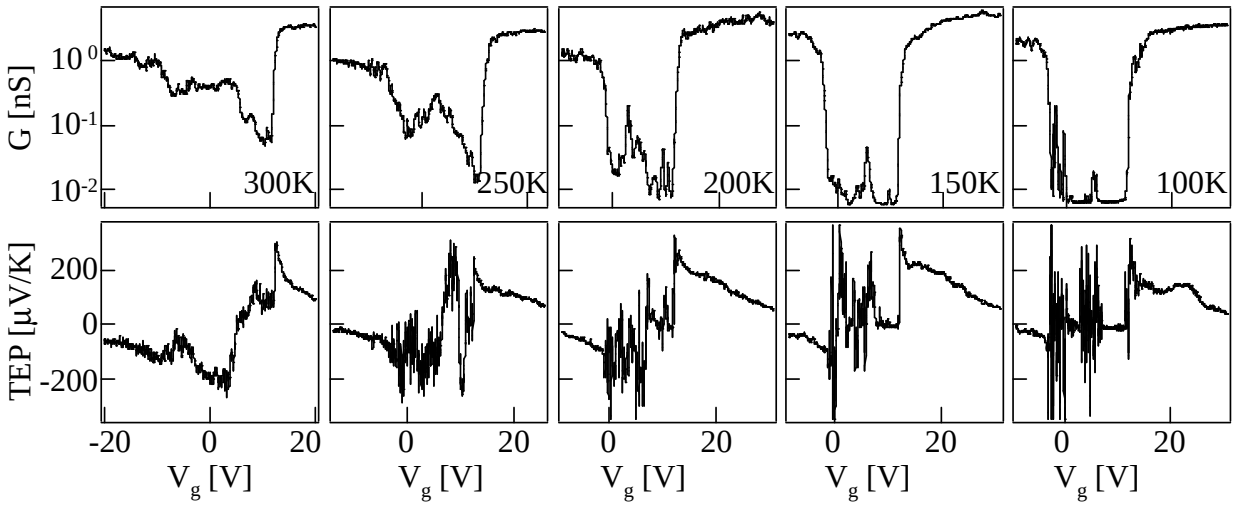

Figure 3.13: Ambipolar G and TEP as a function of Temperature

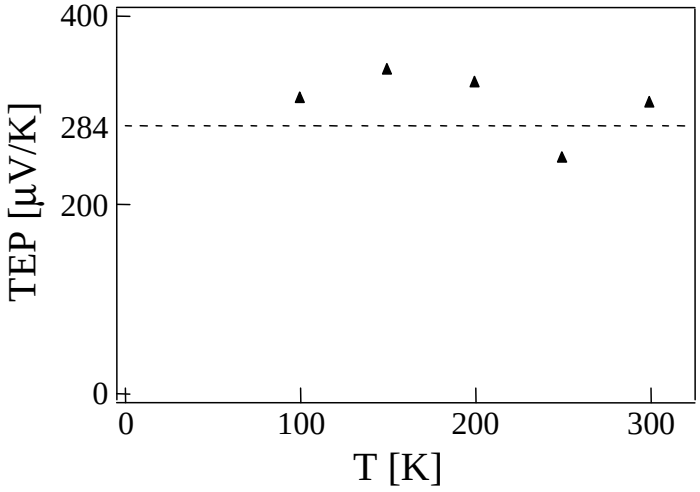

Figure 3.14: Peak TEP in an ambipolar SWNT FET

transport in the FET device. Such nanoscale devices with the capability of producing high TEP are promising for thermoelectric applications.

4 Single-walled Carbon Nanotube as a Quantum Dot

In this chapter we investigate the low temperature transport behavior of mesoscale conductors connected to electrodes by tunnel junctions. Due to their sufficiently reduced geometry, conduction through these devices is controlled by single electron tunneling and is radically different than predicted from Ohm's law. In these systems, the electron-electron (Coulomb) interaction is comparatively strong relative to other energy scales, and free conduction is not possible due to the formation of an electrostatic energy barrier. This situation is referred to in the literature as Coulomb blockade (CB). These devices are named single electron transistors (SETs) or alternatively, quantum dots.

In SETs, transport proceeds through the one-by-one tunneling of individual electrons through the dot. Below we discuss fundamentals of SET behavior (section 4.1), SWNTs as quantum dots (section 4.2), TEP in the Coulomb blockade regime (section 4.3), and results of measuring TEP in the SWNT quantum dot (section 4.4).

4.1 Single-electron Tunneling

In this section, we discuss fundamental characteristics of single electron tunneling. There are many good texts which describe SET behavior, and I follow the presentation given by Tinkham [62]. The interested reader is directed to Grabert [63] for an in depth treatment of Coulomb blockade theory.

In order to measure transport properties of a material, it is usually necessary to electrically contact the material with metallic source-drain electrodes. Often, a tunnel barrier forms at the interface between the electrodes and the material, perhaps due to the formation of a Schottky barrier or existence of an oxide layer. For large, macroscopic materials the device size is such that the capacitive coupling between the electrodes and the material, C, is fairly high. The electrostatic energy

required to add an electron onto the dot, $E_C = e^2/2C$, is small compared to k_BT and no effects due to discrete charge tunneling are observable above the mK range.

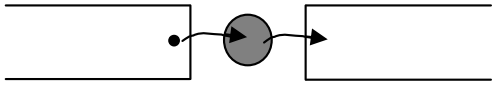

Figure 4.1: Tunneling through a quantum dot

Mesoscopic devices of reduced dimensions typically have a small self-capacitance, and a large corresponding charging energy. At low temperatures, electrons do not have enough energy to overcome this electrostatic barrier, and charge transfer is blocked. Only when the chemical potential of the dot is tuned to particular energy values is charge allowed to tunnel through. Using modern device fabrication techniques it is relatively easy to construct such devices, where single charge tunneling is observable. In order to observe single electron tunneling the charging energy must be smaller than the thermal energy so that the effect is not smeared out by thermal fluctuations. Thus, equation 4.1 states the first of two conditions necessary for a device to exhibit SET behavior.

$$E_C > k_BT \tag{4.1}$$

The second condition concerns the lifetime of the charge state which tunnels onto the quantum dot. Let R be the total tunneling resistance of the quantum dot. For the state to be observable the uncertainty in its energy must be smaller than the energy of the state itself, $\Delta E < e^2/2C$. The lifetime of the charge state on the island is determined by the time scale of the RC circuit, $\tau = RC$. The uncertainty principle demands that $\Delta E \Delta t \geq \hbar \rightarrow (e^2/2C)RC \geq \hbar$. This leads to the second requirement for SET observation (equation 4.2): the total device resistance must exceed the quantum resistance.

$$R \geq \frac{2\hbar}{e^2} \tag{4.2}$$

Under these two assumptions we examine transport through a quantum dot system weakly coupled to source-drain electrodes. A back gate is used to externally modulate the chemical potential inside the quantum dot (figure 4.2).

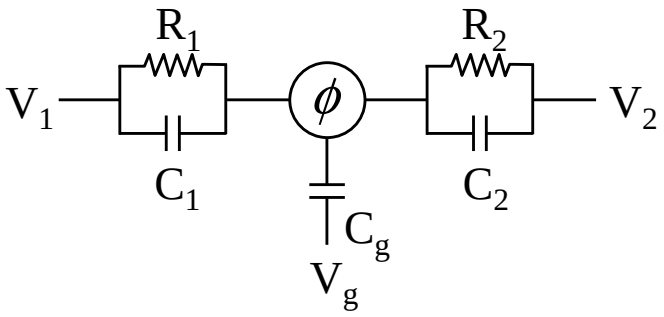

Figure 4.2: Schematic for transport through a weakly coupled quantum dot

We begin by adding electrons to neutral quantum dot until $q_{dot} = -ne$, where e is defined as the charge of a positron. The relationship between the applied external voltages and the potential on the island is derived by summing the charge accumulated on the individual capacitors, $C_i(\phi - V_i)$ and equating it to the charge on the dot, $q_{dot} = -ne$:

$$\phi = \frac{\sum_i C_i V_i - ne}{C_\Sigma} \tag{4.3}$$

where C_Σ is the parallel sum of the capacitive coupling of the quantum dot to the external voltage sources. We now examine the scenario when V_1 and V_2 both approach zero, but the junction is still infinitesimally forward biased. The expression $\Sigma C_i V_i$ reduces to $C_g V_g$, and we determine the total electrostatic energy of the system through simple electrostatics (equation 4.4).

$$U(N) = \int_0^{-Ne} \phi(q')\,\mathrm{d}q' \tag{4.4}$$

Upon substituting for ϕ, it is possible to write the potential energy as a function of the applied external potential and the amount of charge on the dot [62]:

$$U(N) = \frac{(Ne)^2}{2C_\Sigma} + NeC_g V_g \tag{4.5}$$

The total electrostatic energy can now be rewritten in a clever way [63]:

$$U = \frac{1}{2C_\Sigma}(C_g V_g - ne)^2 + \text{const} \tag{4.6}$$

The $C_g V_g$ term is considered an effective charge induced by the gate. One can plot the resulting curves as a function of the total effective charge, $q_{tot} = -ne + C_g V_g$, to determine the transport behavior of the system (figure 4.3).

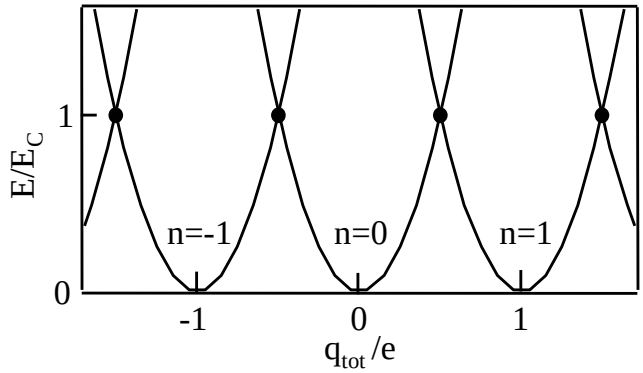

Figure 4.3: Energy of quantum dot as a function of effective total charge

Inspecting figure 4.3, we note that at $V_g = 0$ no charges have accumulated on the dot. Also, when $V_g = 0$ there is a unique minimum in electrostatic energy when $n = 0$ when the temperature is zero. We slowly increase V_g, but still no current is allowed to flow. However, when the gate voltage reaches $V_g = C_g/2e$, the electrostatic energy is the same when $n = 0$ or $n = 1$ electrons are on the quantum dot. This degeneracy is the underlying mechanism which allows charge to flow in the dot.

We now examine transport through the dot upon application of a finite source-drain bias. We set $V_1 = +V$ and $V_2 = 0$ and examine the response of the system at $T = 0$.

First, the total electrostatic energy as a function of N must be recomputed (equation 4.4). From this expression it is possible to solve for the difference in electrostatic energy for an electron tunneling onto $\Delta^+_{1,2} = U_{1,2}(N+1) - U_{1,2}(N)$, or off of $\Delta^-_{1,2} = U_{1,2}(N-1) - U_{1,2}(N)$ the quantum dot via electrode 1 or 2. The

change in electrostatic energy corresponding to a change in charge state $n \rightarrow n \pm 1$ is given by:

$$\Delta E_{1,2}^{\pm} = \frac{e^2}{C_\Sigma}\left[\left[\frac{1}{2} \pm \left(n - \frac{C_g V_g}{e}\right)\right] \pm (-1)^{1,2}\frac{C_{2,1}V}{e}\right] \tag{4.7}$$

for electrons tunneling through electrode 1 or 2 [62]. By positively biasing $V_1 = +V$, tunneling can occur only if either Δ_1^- or Δ_2^+ is negative. One can solve equation 4.7 for values of the voltage, V^*, where $\Delta E < 0$ and charge is allowed to flow through the dot. Graphing V^* as a function of V_g and n, a regular pattern emerges where "Coulomb diamonds" separate different charge states of the island (figure 4.4).

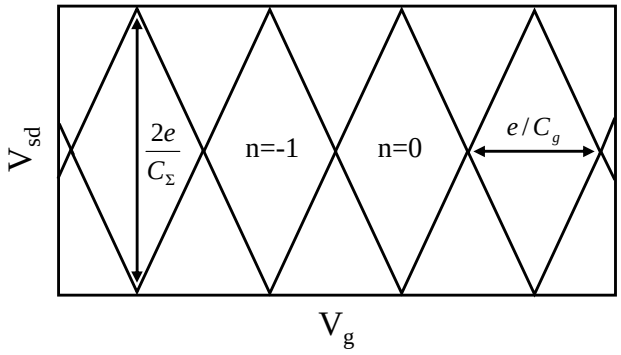

Figure 4.4: SET Stability diagram

The recognizable diamond pattern allows one to extract capacitance values. Fixing $V_{12} = 0$, we can extract the gate capacitance by identifying the period along the V_g-axis as e/C_g. Investigating equations for the critical V^* values separating the $n \pm 1$ charge states identifies the length of the diamond along V_{sd} as $2e/C_\Sigma$. Thus, it is possible to measure the charging energy. As an example, figure 4.5 shows Coulomb blockade diamonds for one of our SWNT quantum dots. The dark regions are areas of low conductance. For this particular dot we extract for the gate capacitance $C_g \sim 15$pF. The charging energy is measured to be roughly $E_C \sim 6$meV.

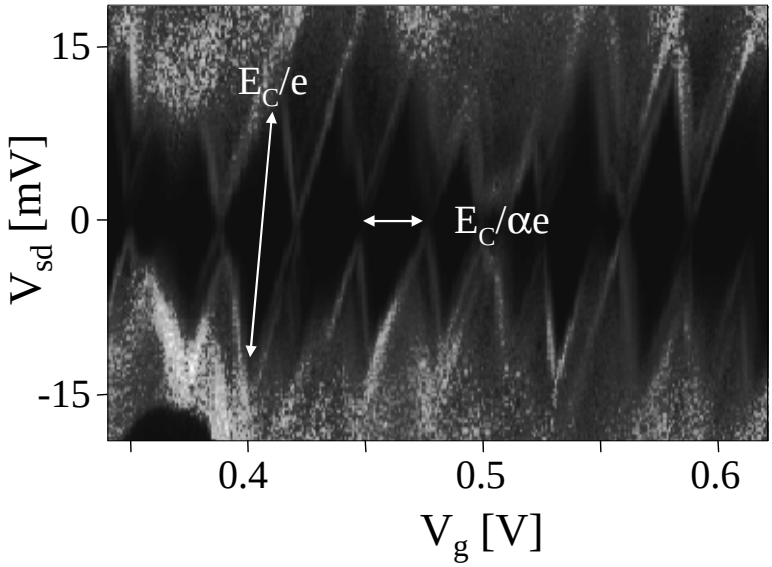

Figure 4.5: Coulomb blockade diamonds

4.2 Single-walled Nanotube Quantum Dot Devices

In the case of classical Coulomb blockade, the energy required to add an electron to the system is equal to the charging energy, $E_C = e^2/2C$. The previous section assumes that the distribution of states is continuous in energy. However, confinement effects in mesoscopic scale devices give rise to a discrete energy spectrum, and the energy required to add an electron to the dot is in fact $E_C + \Delta E$, where ΔE is the level spacing between states in the dot. In this way, investigation of Coulomb blockade transport can yield information about band structure of the material.

In the carbon nanotube the level spacing, $\Delta E = E(k_{n+1}) - E(k_n)$, is computed from the SWNT band structure, where $k_n = n\pi/L$ and n is an integer. The band structure is given by $E(k_n) = \sqrt{E_g^2 + (\hbar v_F k_n)^2}$. In a $L = 1\mu$m long metallic SWNT the level spacing is $\Delta E \sim 1.6$meV. Previously, we examined classical Coulomb blockade where $\Delta E \ll k_B T \ll E_C$. At considerably low temperatures, where $k_B T \ll \Delta E \ll E_C$, effects due to finite ΔE are observable, and it is possible to determine the electronic band structure.

The first observation of Coulomb blockade in carbon nanotubes was made by

Bockrath *et al.*, in 1997 [64]. Since then, numerous efforts to study Coulomb blockade in CNTs were made. Many recent experiments have used this technique to study transport in CNTs [2, 65, 66, 67]. Low temperature transport experiments by Liang *et al.*, were among the first to observe a 4-electron periodic structure in the Coulomb blockade peaks (figure 4.6). The unique structure is explained by the four-fold spin and lattice degeneracy in the carbon nanotube. Consider a nanotube whose "shell" is full. We add to it a handful of electrons, the first of which requires an energy $E_C + \Delta E$ to be added to the quantum dot. Due to the level degeneracy the next three electrons only require E_C to tunnel onto the dot. The fifth electron again requires $E_C + \Delta E$, and the process repeates. This unique 4-electron periodic structure reflects the spin degeneracy of 2 and the lattice degeneracy of 2 in the SWNT.

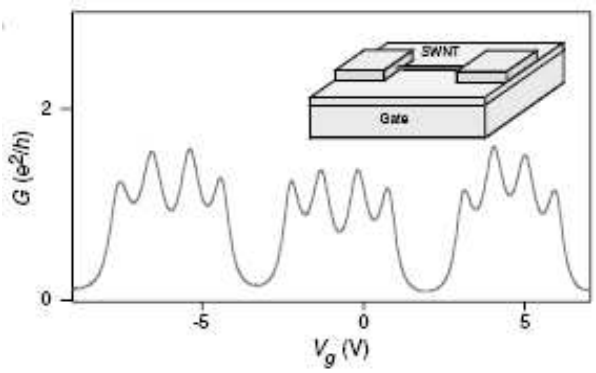

Figure 4.6: Periodic conductance peaks in a SWNT (reproduced from [2])

Additionally, Liang *et al.* observe splitting in the 1st and 3rd conduction peaks under application of a magnetic field. Depending on the "shell" in question the 2nd peak would sometimes exhibit this splitting. This is a signature of Kondo resonance, a many-body interaction effect between electrons in the leads and a localized spin. This observation is explained well by the shell-filling model. The Kondo resonance is only observable when the SWNT quantum dot is in a state of non-zero spin. Thus, the shell-filling then proceeds in either of two ways: $S = 1/2 \rightarrow 0 \rightarrow 1/2 \rightarrow 0$ when the addition of the 2nd electron puts the dot into a singlet state, or $S = 1/2 \rightarrow 1 \rightarrow$

$1/2 \rightarrow 0$ when the dot is in a triplet state [2]. The Kondo effect in SWNTs has also been investigated by Schonenberger *et al.*, [67].

Recently, a number of groups extended CB regime transport to the study of the CNT energy spectrum. Coskun *et al.*, studied band structure of MWNTs under application of a magnetic field, where the NT was converted between metallic and semi-conducting states [66]. Cao *et al.*, probed a suspended SWNT under application of magnetic field. Suspended CNTs are found to exhibit extremely regular Coulomb diamonds, in contrast with data produced by nanotubes lying on the substrate, due to local charge defects in the oxide. At low temperature Coulomb blockade analysis proves to be a powerful method for investigating electronic transport in quantum structures [65]. In the next section we will discuss thermoelectric transport in SWNTs in the CB regime.

4.3 Thermoelectric Power in the Coulomb Blockade Regime

As previously mentioned, Coulomb blockade oscillations of the conductance can yield band structure information by probing the energy addition spectrum. Measurement of TEP in the CB region also produces an oscillatory behavior, and can provide additional transport information to that given by the conductance oscillations. TEP of a quantum dot can describe the energy excitation spectrum [68]. This excitation fine structure appears in both the oscillatory behavior of G and TEP, but is suppressed exponentially by an amount $e^{-\Delta E/kT}$ in the conduction data, and not easily observable. In this chapter we do not address this point further, as our experiments cannot access temperatures low enough to reliably probe the excited states, but note that as a spectroscopic tool, the TEP is quite useful for studying these states.

A detailed theory describing TEP oscillations in the quantum dot was developed by Beenakker and Staring, and is treated within the framework of the orthodox model of single electron tunneling [68]. A qualitative understanding of TEP oscillations of the thermopower is given in the following argument.

Classically, in order to add a charge to the quantum dot, an amount of energy $\Delta E^* = U(N+1) - U(N)$ must be supplied to the system. In a mesoscale system, where energy levels are discrete, an additional amount of energy $E_N - E_F$ must be supplied to fill the next quantum state. Using equation 4.4 we can write down the total energy necessary for conduction through our quantum dot:

$$\Delta E^* = E_N + (N + \frac{1}{2})\frac{e^2}{C_\Sigma} - eC_g V_g - E_F \tag{4.8}$$

E^* oscillates in a sawtooth shape [68], reflecting the order of the tunneling process the system is closest in energy to ($n \to n+1 \to n$ or $n \to n+1 \to n$).

To compute the thermopower in the dot, we follow an argument given by Staring *et al.*[3]. The TEP is calculated indirectly from the Peltier coefficient using the Onsager relations.

$$S = \frac{\Pi}{T} = \frac{1}{eT}\frac{\partial Q}{\partial J} \tag{4.9}$$

Here, Q, is the amount of energy carried by a single electron is calculated as follows. The energy E^* supplied to the system may be used partially to excite an electron in the reservoir to an energy E_1^* above the Fermi level, and partially to create a hole in the dot from a filled state an energy E_2^* below the Fermi level [3]. The total process occurs with probability $e^{-E^*/k_B T}$, and the average energy transported by the electron is $E^*/2$. From equation 4.9 we can calculate the amplitude of TEP oscillation.

$$|S| = \frac{e}{4TC_\Sigma} \tag{4.10}$$

From the behavior of E^*, the thermopower is predicted to oscillate in a sawtooth shape with periodicity identical to the conductance peaks 4.7.

Very few experiments have addressed TEP oscillations in the CB regime. Molenkamp *et al.* demonstrated measurement of thermoelectric voltage 2DEG quantum dots [69, 70, 3], and observed the predicted periodicity in the TEP oscillations (figure

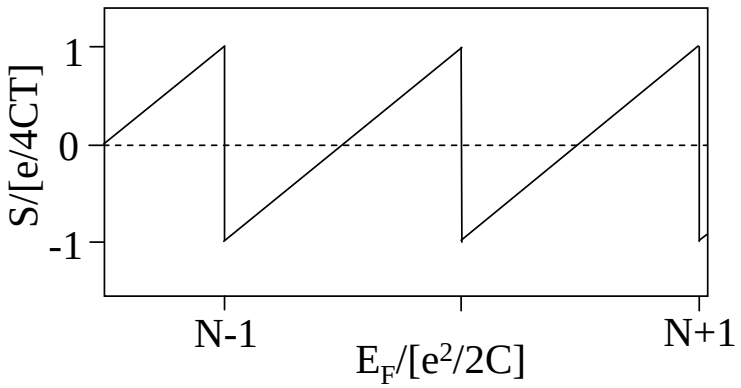

Figure 4.7: Predicted sawtooth oscillations of the TEP

4.8). An AC heating current was passed through a quantum dot defined in a GaAs-$Al_xGa_{1-x}As$ 2DEG while they measured the thermoelectric voltage generated across the dot. Quantitative comparison was not possible since the experiment did not allow for a measurement of the temperature difference, ΔT, across the quantum point contact.

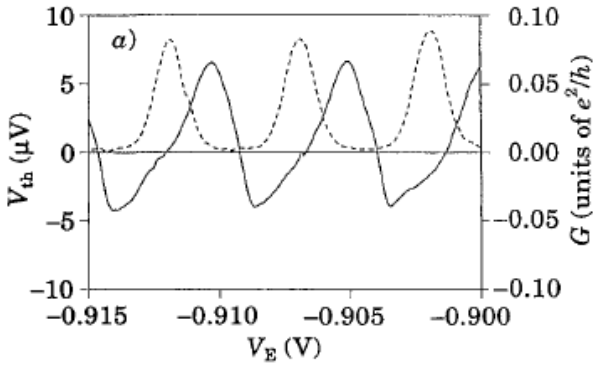

Figure 4.8: Measured G (dashed) and TEV oscillations (solid) in a 2DEG quantum dot (reproduced from [3])

The unique design of our mesoscale TEP device will allow us to quantitatively measure TEP in a CNT quantum dot, and compare it with theoretical predictions.

4.4 Results

We observed Coulomb blockade oscillations in many of our metallic SWNT devices [15]. Simultaneously, Llaguno *et al.*, made similar observations [71]. Onset of the oscillations occurred at temperatures $T \sim 60$K, suggesting a charging energy of roughly $E_C = 6$meV. Figure 4.9 shows data from one such device at $T = 15K$. The data clearly shows a rising slope, and the period of oscillation matches that of the conductance, as expected from Beenakker and Staring's theory described in the previous section.

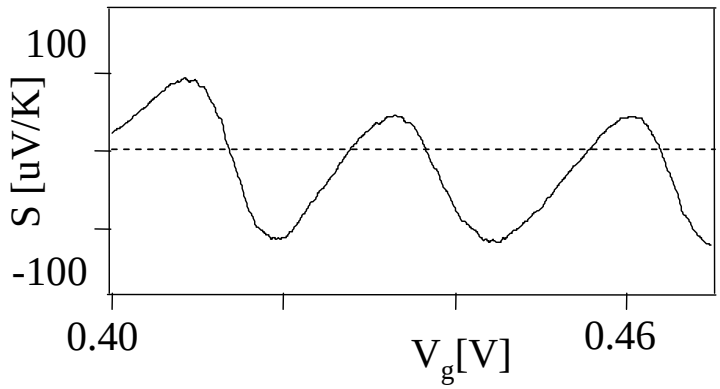

Figure 4.9: Measured Sawtooth oscillations of the TEP in the SWNT

Note that unlike the previous TEP measurements in semi-conducting quantum dots, our TEP measurement in the SWNT carries an exact unit which facilitates a quantitative comparison with theory. To check the temperature dependence of the TEP we swept a large region of the gate voltage from temperatures ranging $T = 300$K down to $T = 4.5$K. Figure 4.10 presents this data for one device. As the device is cooled the conductance decreases and simultaneously develops structure. The TEP also develops a corresponding structure, and oscillations are clearly visible below $T = 30K$.

We plot the average amplitude of the TEP oscillations as a function of temperature in figure 4.11. A clear $1/T$ dependence is observed. By fitting the amplitude of

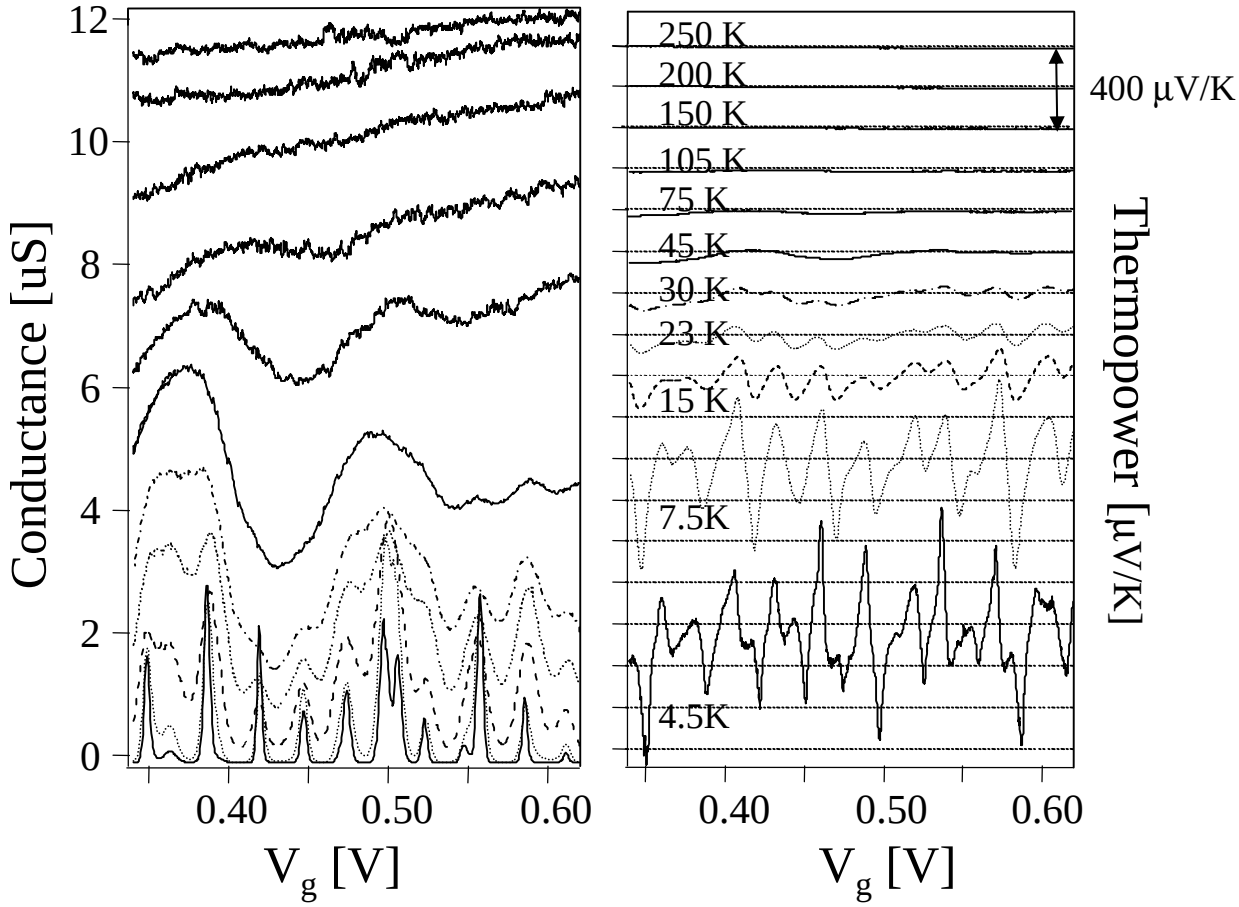

Figure 4.10: Onset of Coulomb blockade in a SWNT

TEP oscillations to $1/T$ using equation 4.10, we extract a value of the charging energy $E_C \sim 3$meV. This differs by a factor of 2 with the value of the charging energy extracted from Coulomb blockade conductance diamonds, $E_C \sim 6$meV. The origin of this difference is unclear, but we speculate that charge traps in the oxide breaking up the nanotube into multiple quantum dots, coupled with hysteresis between the Coulomb diamond measurements and the TEP measurements.

In conclusion, we measured the TEP oscillations in our SWNT quantum dot and found both the shape and amplitude of the oscillations to be in good agreement with theoretical predictions. We observed quite large values of the TEP ($\sim 500\mu V/K$), and were able to tune the TEP values by modulating a back gate voltage. Due to the reduced geometry of the SWNT, the onset temperature of Coulomb blockade

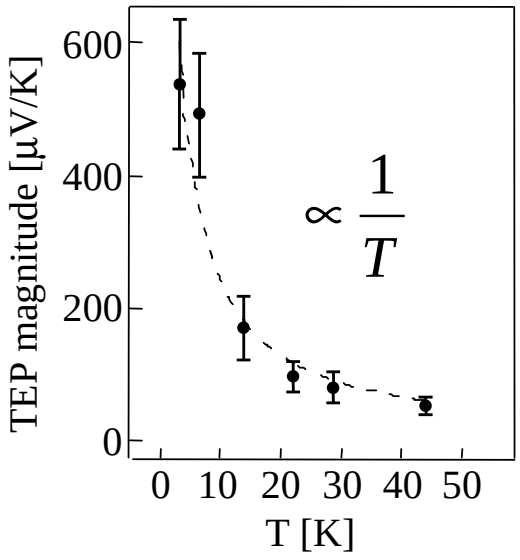

Figure 4.11: Amplitude of TEP oscillations as a function of T

was relatively high, at $T \sim 60K$.

5 Thermoelectric Transport in Multiwalled Carbon Nanotubes

Multi-walled nanotubes (MWNTs) composed of closely nested SWNT shells are a complex material on which disagreements regarding fundamental transport properties still exist. Measurements are still in conflict on the number of conducting shells, the number of occupied subbands, the doping state, and whether transport is diffusive or ballistic. Measurements of the thermopower in the MWNT indirectly allow us to probe the density of states and gives insight into some of these unresolved issues. In this chapter we discuss the current state of transport in the MWNT 5.1 and then we interpret the results of our TE measurements 5.2

5.1 Electronic Transport in MWNTs

In principle electrical transport in MWNTs is quite simple. The total conductance, G, should be simply the parallel sum of the contributions due to each shell: $G = \sum_i G_i$. However, actual MWNT response is complicated by shell-shell interactions, shielding by other shells, and the nature of contact to the MWNT (plane or top-down). A wide range of transport experiments have addressed conduction in MWNTs with sometimes conflicting results.

Frank, et. al, designed a unique experiment to probe the electrical properties of the MWNT [72]. The experiment involved mounting an individual MWNT on the tip of a scanning probe microscope and repeatedly dipping it into liquid Hg, serving as an electrode. The SPM tip acted as the other electrode. They found conductance to be exactly e^2/h for all MWNT samples, indicating ballistic conduction in one mode. The experiment was independently performed by Urbina et. al, [4], where this time the conduction was measured to be $2e^2/h$, suggesting two-mode conduction only through the outermost shell (figure 5.1). The factor of two discrepancy has not been sufficiently explained, but these two experiments have been frequently cited as evidence for ballistic transport in MWNTs.

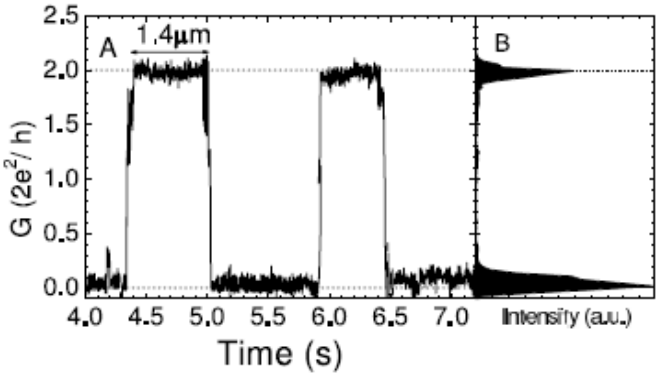

Figure 5.1: MWNT SPM conductance measurements (reproduced from [4])

Shortly after, evidence supporting diffusive conduction was presented. Bachtold et. al, performed an Aharonov-Bohm type experiment where conduction in the MWNT was measured as a function of an axially directed magnetic field [5]. In a conductor, an electron retains a slightly higher probability of remaining in its original location rather than traveling elsewhere due to the constructive interference between paths which form a closed loop and their time-reversed counterparts. This phenomenon is known as weak localization (WL). The Aharonov-Bohm experiment demonstrates existence of weak localization by applying a magnetic field and destroying time-reversal symmetry. This leads to an increase in conductance under application of a magnetic field. Additionally, the conductance should oscillate as a function of magnetic flux with period $h/2e$. Figure 5.2 shows the results of the Bachtold, *et al.*, experiment. The periodicity allows extraction of magnetic flux which corresponds to flux through a cylinder with diameter equal to that of the MWNT. This suggests transport occurs through the outermost 1-2 shells. Importantly, diffusive conduction, or back scattering of electrons, is essential for interference of the quantum mechanical paths. The existence of WL in the MWNT provides support for the diffusive transport picture.

With the observation of universal conductance fluctuations (UCF) in MWNT's, support appears to be stronger for the case of diffusive transport, however the issue is not yet settled completely.

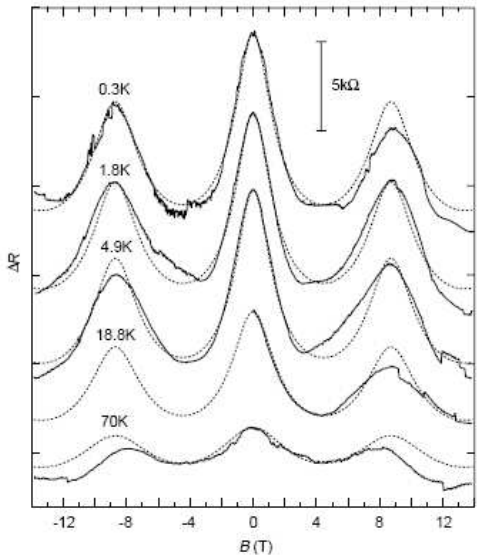

Figure 5.2: Aharonov-Bohm in MWNT (reproduced from [5])

We now address the topic of number of conducting shells in the MWNT. Zettl's group has made non-local IV measurements which support the claim that very few (1-2) shells carry current in a typical MWNT device [6]. Briefly, in this experiment current is applied between a pair of contacts displaced by a distance, x, from another pair of contacts used to probe the non-local voltage drop. An exponential dependence on the separation between the measurement sites (figure 5.3) allowed Bourlon *et al.*, to extract a length scale of approximately $l \sim 1\mu$m. It is argued that current from one shell reaches the next shell on the order of this length scale, suggesting only 1-2 outermost shells carry current in 1μm scale devices.

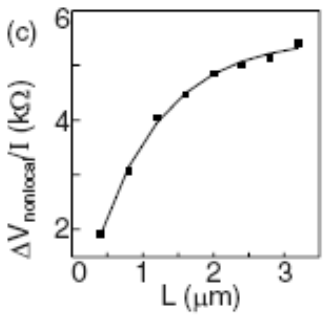

Figure 5.3: Non-local IV measurements (reproduced from [6])

Also in support of this "few-shell" conduction model are the previously described SPM experiments [4, 72] where conductance appears to be quantized in units of e^2/h or $2e^2/h$ at room temperature. While the Aharonov-Bohm experiment [5] seems to offer evidence in support of this model, the experiment was performed at $T = 70$K where previously conducting inner shells are likely to have been frozen out.

While most of the previously mentioned MWNT experiments have indirectly inferred the number of conducting shells, Collins *et al.*, have devised a method whereby the outermost shells can be removed one-by-one, and the MWNT electrically characterized at each step [7, 8, 73]. The outer layer is selectively removed by high-bias controlled electrical breakdown, and then characterized by measuring G as a function of V_g. Figure 5.4a shows the high-bias behavior of conductance as the shells are removed. From this data, Collins *et al.*, contend that each shell carries an amount of current roughly $I \sim 12\mu$A [7]. Figure 5.4b gives the low-bias MWNT behavior. It is clear from the data that at room temperature ~ 10 shells contribute to the conduction at room temperature [8].

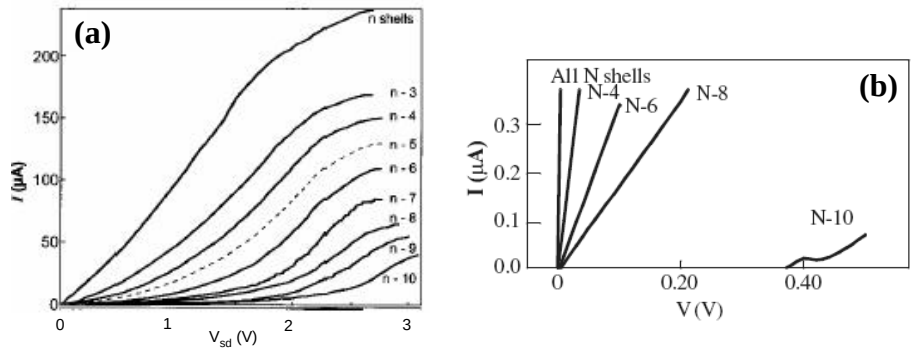

Figure 5.4: Controlled breakdown in MWNTs (reproduced from [7] (a) and [8] (b))

Although many of the reports described in this section conflict with one another, it is clear that there are many interesting remaining questions regarding MWNT transport. In the next section we describe how TEP measurements can help answer some of these questions and discuss the results of our experiment.

5.2 Results

Thermoelectric power measurements can provide a unique experimental probe for investigating the electric transport properties of MWNTs. Coupled with conductance measurements, TEP measurements in SWNTs showed that the measured TEP can be closely related to the change of electrical conductance, which is readily modulated by the gate voltage [15]. In MWNTs, the comparison of mesoscopically measured G and TEP can be employed to probe the inter-shell coupling, by measuring effective gate coupling to the MWNT as a function of temperature.

In this section we present the results of our electric field modulated G and TEP measurements in MWNTs. Comparison of conductance to the measured TEP at various temperatures provides a way for determining the density of states in the MWNT, and indirectly the number of current carrying shells of single sub-band occupation.

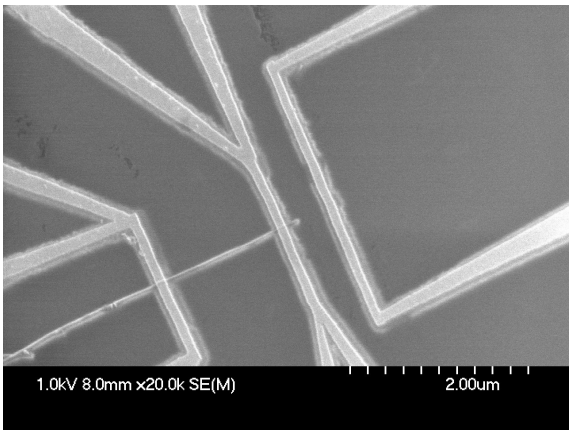

Figure 5.5: SEM image of a typical MWNT device

The MWNTs used in this experiment have diameters ranging d=8-12nm, and were obtained from the arc discharge method [74]. The MWNTs were suspended in chloroform and spin cast onto a silicon/silicon oxide wafer with predefined alignment markers. The fabrication procedure followed that of the SWNT TEP device 3.2, except in choice of contact metals which were changed to 5 and 30nm of Ti and Pd, respectively, due to the improved contact resistance. An SEM image of a

typical MWNT is shown in figure 5.5. To measure TEP in the MWNT we used the techniques described for SWNT measurement (section 3.3).

In this experiment we have measured the conductance and TEP of approximately 10 individual MWNT samples as a function of applied gate voltage and temperatures ranging from 15K to 300K. Device transport characteristics allow us to classify the MWNTs into two broad catagories: (i) metal dominated (m-MWNT) and (ii) semi-conducting dominated (s-MWNT). For m-MWNTs, the gate voltage dependent conductance, $G(V_g)$, shows no appreciable changes at high temperature and it remains finite even at low temperatures, indicating at least one metallic SWNT shell near the outer diameter of the MWNT is dominate in the electric transport. Figure 5.6b shows typical room temperature and low temperature transport characteristics of such a m-MWNT. On the other hand, in s-MWNTs, $G(V_g)$ shows an appreciable dip at room temperature which develops into a gap ($G = 0$) as temperature decreases, indicating that the Fermi energy sweeps through the band gap region of the outer shells of the MWNT as V_g changes (Figure 5.6b). We found m-MWNT as the dominant species (8 of 10) while only 2 of 10 devices exhibited s-MWNT characteristics. Considering the fact that all the outermost current carrying shells must be semiconducting SWNT shells in order to exhibit s-MWNT characteristics, the rare occurrence of s-MWNTs is understandable.

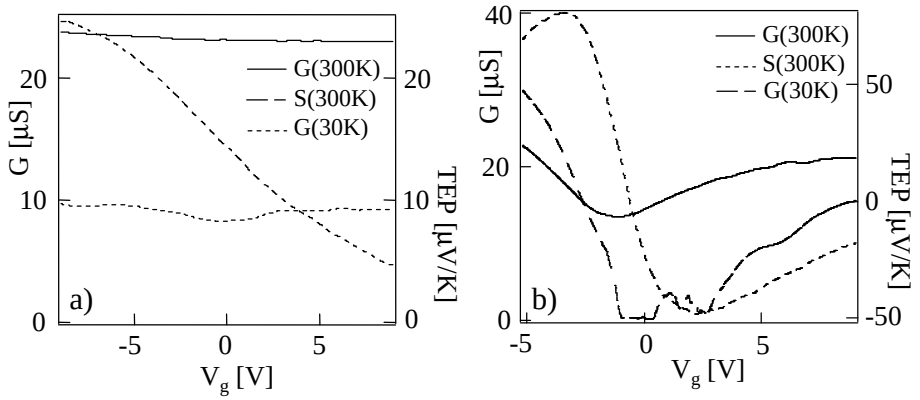

Figure 5.6: m-MWNT (a) and s-MWNT (b) at high and low temperatures

The measured room temperature TEP of m-MWNTs and s-MWNTs exhibit distinct differences which further substantiate the classification introduced above. While for m-MWNTs the TEP varies over $\sim 25\mu$V/K range and typically exhibits a downward sloping curve (dotted line in Figure 5.6a), the TEP is large and anti-symmetric about $V_g = 0$ in the s-MWNT. On a qualitative level this behavior can be explained by the Mott formula. Specifically, for s-MWNTs the Mott formula explains the severe sign change in S as $G(V_g)$ exhibits a dip in the band gap region. However, for a quantitative comparison, we must take into account the multi-channel transport nature of the MWNT. For, m-MWNTs exhibit rather unexpectedly large TEP considering the relatively slight p-type conductance curves. It is speculated that this TEP is contributed from semi-conducting shells deep within the MWNT indicating that contributions to $S(V_g)$ and $G(V_g)$ by the different subshells might be weighted in a particular way.

In order to discuss the relationship between G and TEP, it is now necessary to mention a general property of thermoelectric measurements in multi-channel conductors. For N independent non-interacting channels in parallel, simple analysis gives that the total TEP should be the sum of individual TEP for each channel weighted by its conductance:

$$S = \sum_i \frac{G_i S_i}{G_{tot}} \tag{5.1}$$

where G_i and S_i are the electric conductance and thermopower of the i^{th} channel and $G_{tot} = \sum_i G_i$. Combining this equation with the Mott formula 5.2:

$$S = -\frac{\pi^2}{3}\frac{k^2 T}{e}\frac{d\ln G}{dE} \tag{5.2}$$

we can now separate the transport contributions from the semi-conducting shells and metallic shells.

For example, the data shown in Figure 5.7 illustrates this separation in the measured conductance (a) and TEP (b) in a typical m-MWNT (d=10nm). In this MWNT the conductance exhibits a flat metallic background while the weak p-type

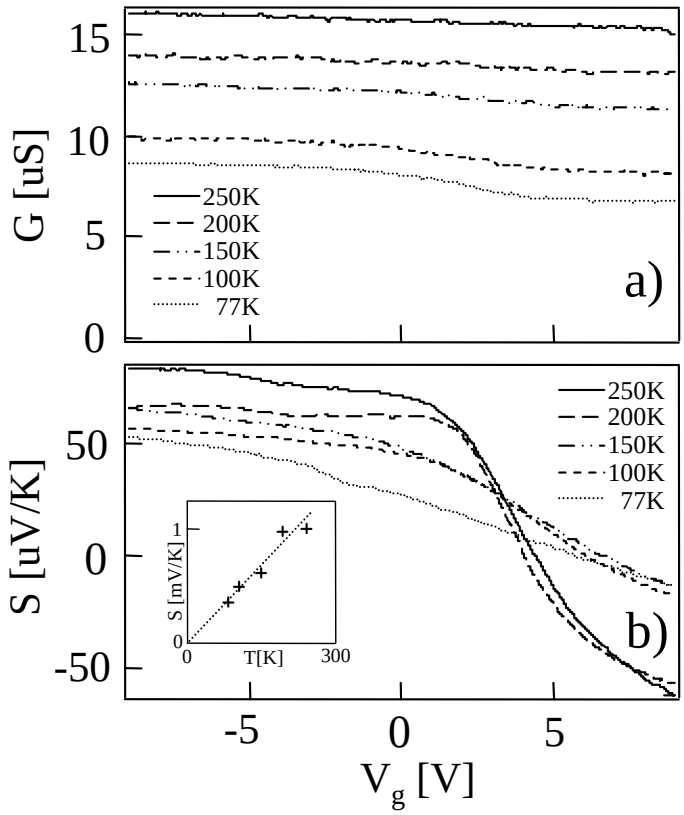

Figure 5.7: $G(V_g)$ (a) and $S(V_g)$ for a m-MWNT

semi-conducting shell contribution becomes more pronounced at low temperatures. For simplicity, we assume that the total conductance and TEP contributions from all metallic (semi-conducting) shells in this MWNT are G_m (G_s) and S_m (S_s) respectively. At large positive gate voltages, $V_g \gg 0$, the semi-conducting shells are expected to turn off and the only contribution to $G(V_g)$ in this regime is due to G_m. Assuming $G_m(V_g)$ is constant in temperature, we can extract $G_s(V_g)/G(V_g)$ from the data. This ratio allows the evaulation of S_s from the Mott formmula. The inset to figure 5.7b shows the estimated $S_s(V_g = -10V)$, where we observe TEP as large as 1mV/K at T=300K. It is interesting to note that the temperature dependent S_s appears linear in T (solid line in inset to figure 5.7). This behavior was discussed in the TEP of semi-conducting SWNTs connected to electrodes through a potential barrier Δ, where the saturated TEP is described by tunneling through the barrier

in the WKB approximation scheme [15]: $S_s = \frac{\pi^2 k_B^2 T}{6|e|\Delta} ln \frac{G(\Delta=0)}{4e^2/h}$.

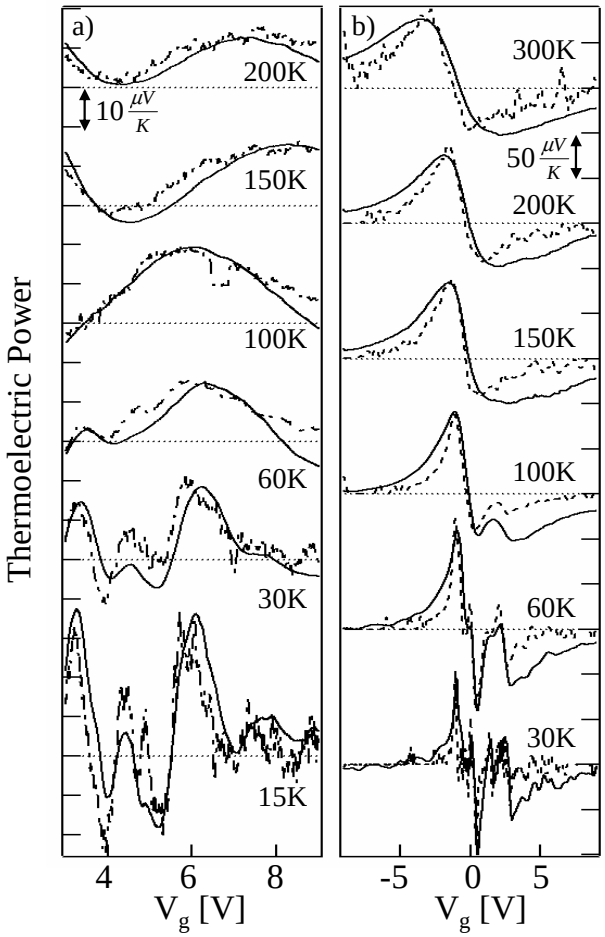

Figure 5.8: Measured (solid) and calculated (dashed) TEP for a m-MWNT (left) and s-MWNT (right)

We now turn our attention to quantitative comparison of measured TEP to the conductance. Figure 5.8 shows the measured TEP for a representative m-MWNT (figure 5.8a) and s-MWNT (figure 5.8b). In particular, we chose a m-MWNT that shows an appreciable variation in $G(V_G)$ in the $V_g > 0$ region, where the semiconducting shell contribution is minimal. We note that in this regime the change in chemical potential dE induced by the gate voltage change dV_g is related by $C_g \Delta V_g = \rho_{MWNT} \Delta E$, where ρ_{MWNT} is the density of states in the MWNT and C_g is the gate capacitive coupling. This linear relation now allows a direct comparison

between measured $G(V_g)$ and $S(V_g)$ via the Mott formula. The broken lines in figure 5.8 display $-\alpha d\ln G/dV_g$ scaled by a single fitting parameter $\alpha(T)$. Excellent agreement between measured TEP and calculated diffusion TEP is found using the Mott formula (equation 5.2) for temperatures ranging from 15K to 300K, indicating that the Mott prediction works well up to a factor α.

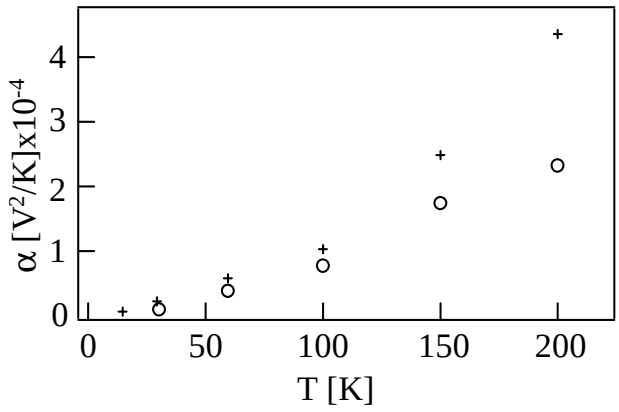

Figure 5.9: $\alpha(T)$ in a m-MWNT (cross) and s-MWNT (circle)

The scaling factor $\alpha(T)$ (figure 5.9) in the above analysis can be used to estimate the number of SWNT shells participating in conduction at a given temperature. From the direct comparison with equation 5.2 we obtain:

$$\alpha = \frac{\pi^2}{3}\frac{k_B^2 T}{e}\frac{\rho_{MWNT}}{C_g} \tag{5.3}$$

Here $C_g = 2\epsilon\epsilon_0/\ln(2h/r)$ considering the device geometry, and $\rho_{MWNT} = N_{eff}\rho_{SWNT}$, where N_{eff} is the effective number of current carrying shells and ρ_{SWNT} is the density of states for a SWNT shell. Capacitive values were calculated to be $C_g^{12nm} \sim 45$pF/m and $C_g^{5nm} \sim 37$pF/m for the MWNTs in (a) and (b), respectively. Since we consider only metallic SWNTs or large diameter/small band-gap semi-conducting SWNTs, we take $\rho_{SWNT} = 8e/hv_F$, where the Fermi velocity is $v_F = 8 \times 10^5$m/s in the CNT.

Figure 5.10 shows the resulting N_{eff} for the MWNTs in figure 5.8. A clear trend of decreasing N_{eff} is found as T decreases. For the MWNTs we measured, similar

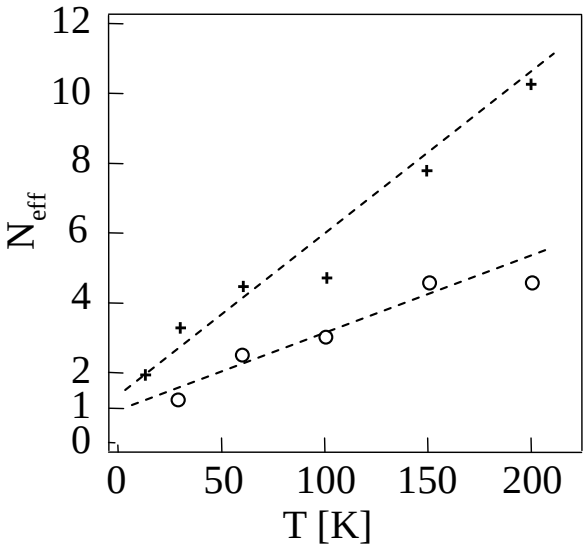

Figure 5.10: Effective number of shells in m-MWNT (cross) and s-MWNT (circle)

analysis shows that $N_{eff} \sim 5 - 10$, indicating that multiple outer NT shells participate in conduction at room temperature, while $N_{eff} \sim 1$ at lower temperatures ($T < 30K$). This is in good agreement with controlled breakdown experiments [7, 8]. Directing our attention to the low temperature portion of the graph, we notice that the intercept is roughly equal to 1 for each device, corresponding to only 1 shell actively participating in transport.

In conclusion, TEP measurements are a useful means to characterize and probe transport in the MWNT. In conjunction with conductance measurements they allow for a unique method to probe the MWNT density of states. Further study of the temperature dependence of the number of conduction shells may allow investigation of the inter-shell coupling.

6 Thermoelectric Transport in Silicon Nanowires

The reasons attributing to the recent explosion of interest in 1d materials are twofold: 1) to further understanding of fundamental low-dimensional systems; and 2) for use in future nanoelectronic applications. Thus far we have concerned ourselves only with carbon nanotubes, yet semi-conducting nanowires form another broad class of materials under heavy investigation. Nanowire variety is as wide as the variety of the underlying material. Recently, there have been reports on synthesis and transport in Si [75], Ge [76], InP [77] and other types of nanowires. We examined electric and thermoelectric transport in one of these species: the Silicon nanowire (SiNW). In this chapter we discuss electron transport in SiNWs (section 6.1), device fabrication (section 6.2), and then present our results (section 6.3).

6.1 Electronic Transport in SiNWs

Silicon nanowires exhibit numerous properties which make them excellent candidates for future nanoelectronic applications. First, their lateral size is small enough that they can effectively be considered one dimensional. In fact, the recent demonstration of $d = 3$nm SiNW growth [78] highlights that the SiNW diameter is now approaching that of the SWNT. Second, these semi-conducting nanowires exhibit FET behavior, and transistor action in SiNWs has been demonstrated in Lieber's group [75]. Third, their ability to be controllably doped is crucial for practical use in emerging technologies. Electrical transport measurements were reported on doped SiNWs as early as 2000 by Cui *et al.* [75]. Since then, there followed improvements in fabrication allowing the creation of high performance SiNW FETs [79], and the demonstration of more complex electrical devices (the pn junction [80]).

Furthermore, in addition to these properties, their are advantages in SiNW synthesis upon comparison with that of carbon nanotubes. While the length and diameter of CNTs are under reasonable control, growth of CNTs with specific electrical properties has never been realized. The diameter and helicity, which are crucial to the CNT's electronic properties, cannot be selected beforehand. CNT growth

produces for the experimenter a mixture of metallic and semi-conducting devices of varying diameter. SiNW growth, however, is much better controlled [75, 81]. All devices are naturally semi-conducting, and the nanowire diameter distribution falls tightly around the growth catalyst particle diameter [9, 78]. Thus, SiNW's are more readily accessible than CNT's as nanoelectronic components since they have already circumvented the controlled growth problem.

Motivated by the SiNW's strong potential as a nanoelectronic device, much work was done on characterizing its electrical properties. Cui *et al.*, doped SiNWs and reported the first measurements of such systems [75]. Both p- and n-type devices were fabricated through by flowing B and Ph gas during the laser assisted catalytic growth and were contacted with Al/Au electrodes. Gate-dependent transport measurements allowed extraction of the mobility from the transconductance [33, 75]

$$\frac{\mathrm{d}G}{\mathrm{d}V_g} = \mu \frac{C}{L^2} \tag{6.1}$$

where the geometrical capacitance is estimated from a cylinder on a plane model $C \sim 2\pi\epsilon\epsilon_0 L/\ln(2h/r)$. The extracted mobilities for these early devices were quite low, on the order of 1 $\mathrm{cm}^2/\mathrm{Vs}$ for B-doped SiNWs.

By changing to a Ti contact metal, Cui *et al.*, demonstrated improvements in device performance as Ti forms a stable conducting silicide with p-type silicon [34, 82]. Thermal annealing shifted the average two-terminal resistance from $R = 160\mathrm{M}\Omega$ before annealing, to $R = 620\mathrm{k}\Omega$ after annealing. This was attributed to formation of a better metal-semi-conductor contact and passivation of defects at the $\mathrm{Si} - \mathrm{SiO}_x$ interface [82]. Chemical passivation of the SiNW device led to a 2 order of magnitude improvement in mobility. After the surface chemistry (4-nitrophenyl octadecanoate treatment) average mobility improved from $\mu = 30\mathrm{cm}^2/\mathrm{Vs}$ to $\mu = 560\mathrm{cm}^2/\mathrm{Vs}$. This was attributed to passivation of defects which compensate applied gate voltage by trapping and scattering carriers [82]. In addition to improved device characteristics transport also became more stable. Conductance curves became more reproducible and less hysteretic.

Zheng *et al.*, examined SiNW transport quantities as a function of doping through creation of high performance n-type SiNW devices of varying phosphorous concentration [79]. 4-probe conductance measurements revealed the strong role that contact resistance plays in these devices. The apparent problem of decreasing mobility with decreasing dopant level was resolved after extracting mobilities from gate-dependent 4-probe conductance measurements, rather than the 2-probe quantities. Device mobilities from 95 to 260cm$^2/Vs$ were reported [79].

Recently, Zhong *et al.*, reported low temperature measurements on p-type SiNW's [83]. Observation of single electron tunneling through discrete levels suggests that transport in these $L = 400$nm devices is coherent. In addition, magnetic field dependent Coulomb blockade measurements allowed examination of the ground state spin configuration, which alternates between $S = 1/2$ and $S = 0$ [83].

For the most part, experimental measurements on SiNW's have so far described transport quantities without commenting heavily on the transport mechanism (e.g, SB or bulk controlled). Although, recently Ahn *et al.*, have performed a very interesting experiment which can spatially probe the SiNW electronic band structure [84]. Scanning gate photoelectronic (SGP) measurements allow spatial measurement of the band structure by locally exciting electron-hole pairs and measuring the resulting photocurrent. Their SGP measurements provide evidence of strong gate-dependent Schottky barrier band bending near the contacts.

In addition to these electrical measurements, the thermal conductance of SiNW's has also been measured [20]. However, to date no thermoelectric measurements have been performed on SiNW's. Thermoelectric power measurements can illuminate the SiNW transport mechanism by supplementing the results provided by electrical measurements.

6.2 Device Fabrication

We now turn our attention to thermoelectric device fabrication. Our SiNW samples were synthesized in C. M. Lieber's group at Harvard by Zhaohui Zhong and Ying

Fang using the vapor-liquid-solid (VLS) method described in references [9] and [78]. Briefly, $d = 10$nm Au catalyst particles are distributed on a SiO_2 substrate and inserted into a chemical vapor deposition furnace. Silane (SiH_4) acts as a vapor phase reactant, along with B_2H_6 which Boron dopes the SiNW's, leading to p-type behavior. The gas flow rates lead to a nominal doping of $5.3 \times 10^{20}\text{cm}^{-3}$. Lieber's group has characterized the VLS grown SiNW's by TEM and found that their crystal growth orientation is a function of NW diameter. Small diameter SiNWs ($d \leq 10$nm) grow axially in the $\langle 110 \rangle$ direction (Figure 6.1), whereas larger diameter wires ($d \geq 20$nm) grow in the $\langle 111 \rangle$ direction [9].

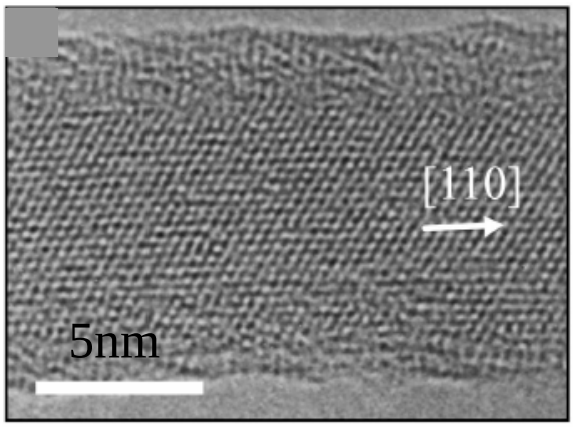

Figure 6.1: d=10nm SiNW growth direction (reprodeced from [9])

The nanowires are then suspended in ethanol. The nanowires are transferred from solution via pipet to a Si/SiO_2 oxide substrate with preexisting alignment markers (Figure 6.2). A thermoelectric device similar to that described in section 3.2 is patterned on top of the SiNW by electron beam lithography. After development, a $t \sim 5s$ HF etch removes the outermost SiO_x layer immediately before metal deposition. This is found to create better electrical contact to the device. There follows metal evaporation of Ti (2nm) and Pd (40nm).

After lift-off in acetone the device is electrically characterized using a probe station. On-state resistance values ranged $5 - 100\text{M}\Omega$. Rapid thermal annealing

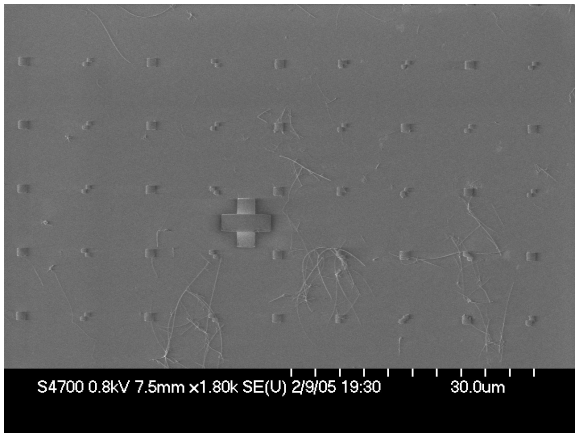

Figure 6.2: SiNW's distributed on predefined alignment markers

at $T = 250^{o}$C for $t = 5$min in forming gas (10% H_2, 90% He) improved the on-state resistance to $250\text{k}\Omega - 20\text{M}\Omega$. Figure 6.3 presents a typical change in device characteristics as a result of thermal annealing.

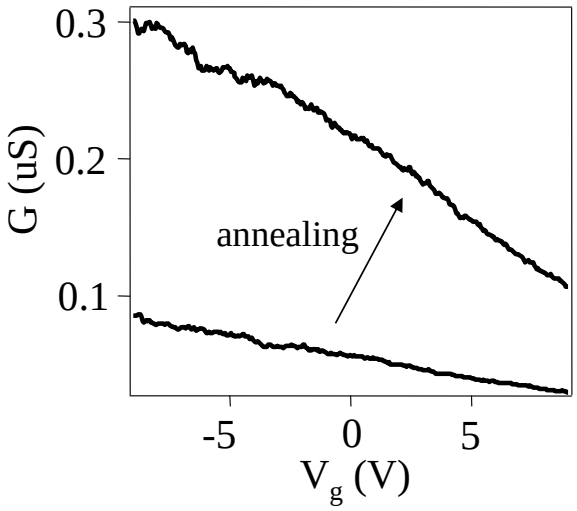

Figure 6.3: Conductance of a typical SiNW device before and after rapid thermal annealing

The sample is then wirebonded and immediately inserted into a Janis continuous flow cryostat for measurement.

6.3 Results

In this section we present the results of our thermoelectric power measurements on the SiNW devices. TEP, conductance, and calibration measurements were performed as a function of temperature and gate voltage. We followed the measurement techniques described in section 3.3. Conductance was measured using a small ($V_{sd} \ll k_B T$) source drain bias voltage along with a Keithley logarithmic current amplifier. The TEP was measured using a high input impedance differential voltage amplifier in conjunction with a Stanford Research (SR830) lock-in amplifier. In order to measure as deeply as possible into the turn-off regime, the TEP and conductance were measured separately so that the input impedance of the measurement configuration was a maximum. This has the drawback of not being able to align the G and TEP measurements with one another as a function of gate voltage, as hysteresis allows the turn-on voltage to change. We did find large hysteretic behavior in our sample, however this does not greatly affect interpretation of our results as the on-state, subthreshold regime, and off-state are all visibly separable from one another in both TEP and G plots.

Figure 6.4 shows the conductance as a function of V_g for temperatures ranging 80K to 260K. Conductance curves were shifted in gate voltage for clarity. Mobility for this sample was roughly $\mu \sim 17\text{cm}^2/\text{Vs}$ at room temperature. Typical mobilities for our SiNW devices ranged from $0.1 - 20\text{cm}^2/\text{Vs}$, somewhat lower than the mobilities reported by Lieber's group. This is to be expected, as we did not perform the 4-nitrophenyl octadecanoate surface chemistry which might passivate local charge traps in the oxide layer of the nanowire [82].

We present V_g dependent TEP measurements for the same device as a function of temperature 6.5. At first glance, the SiNW TEP profile looks similar to that of the semi-conducting SWNT. We note large saturated TEP values in the on-state which decrease with decreasing temperature, and a rise in the TEP as the device turns off. However, in the CNT, the TEP rises to a value of $S \sim 284\mu\text{V/K}$ independent of the temperature. In the case of the SiNW, this value clearly decreases as the

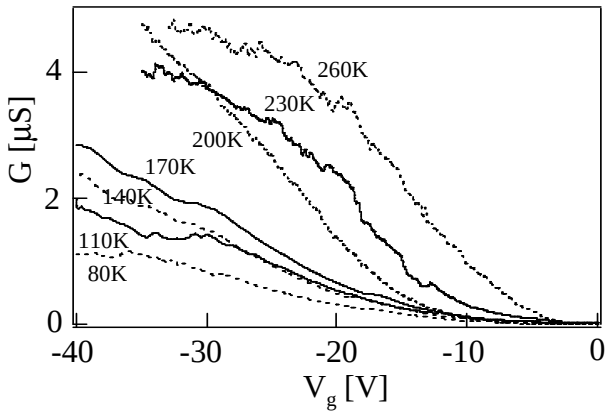

Figure 6.4: $G(T)$ vs V_g for a typical SiNW device

temperature is lowered.

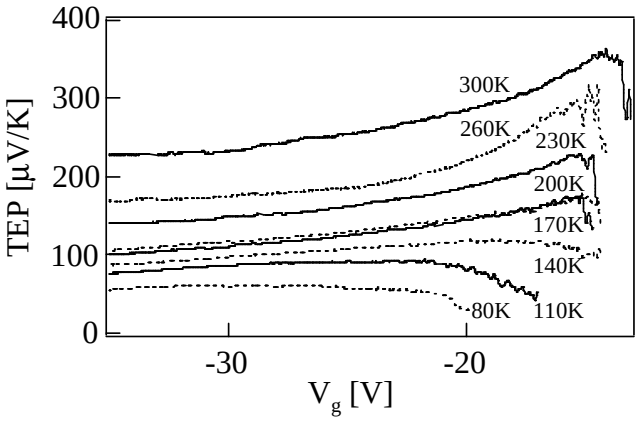

Figure 6.5: $S(T)$ vs V_g for a typical SiNW device

This TEP behavior is not particular for this device, but is seen in all of our SiNW devices. Figure 6.6 plots AC and DC measurements of TEP for two additional SiNW devices. Still, the room temperature peak value hovers around $S \sim 300\mu$V/K and decreases with decreasing temperature.

We also observe similar saturated TEP behavior in the on-state of the other SiNW devices. The saturated TEP seems device independent, and we plot the on-state TEP value as a function of temperature for all 5 SiNW devices which we measured in figure 6.7.

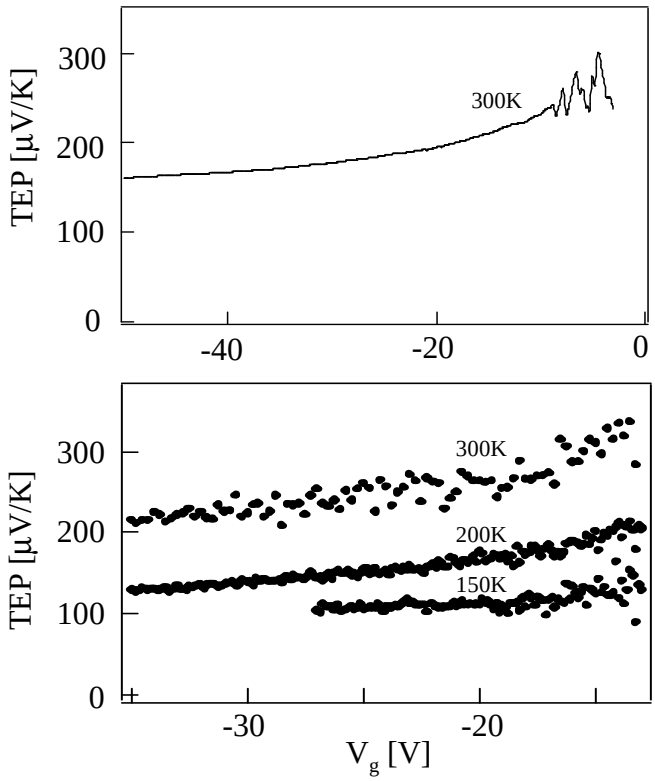

Figure 6.6: DC (bottom) and AC (top) measured S vs V_g for additional SiNW devices

The saturated TEP values fall on a line of slope $\mathrm{d}S/\mathrm{d}T \sim 0.67T[K]\mu\mathrm{V/K}$ and intercept roughly zero.

We attempt to explain these findings through use of a simple model based on series transport through Schottky barriers and bulk Silicon. Figure 6.8 shows the proposed energy band diagram for a SiNW FET when the device is beginning to turn on. The total length of the device is L, but we divide the nanowire into two distinct spatial regions: x_b is the "bulk" Silicon NW length, and x_{SB} is roughly the "Schottky length" of the NW.

We assume that the temperature gradient due to the heater falls linearly across the substrate according to $T = T_0 + \frac{L-x}{L}\Delta T$, where x is measured from the source electrode, and ΔT is the total applied temperature difference across the device. We then solve for the thermopower, S, for the case of two materials in series, as it was

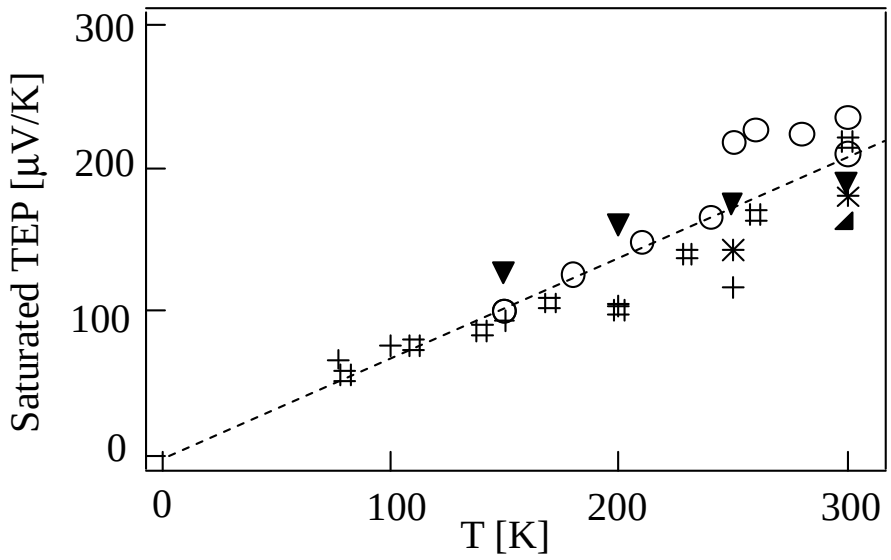

Figure 6.7: on-state SiNW TEP as a function of Temperature

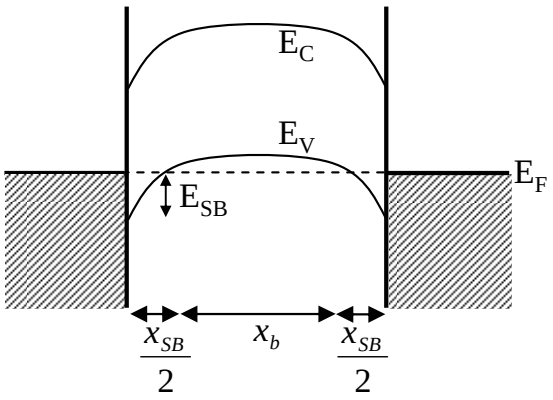

Figure 6.8: Schottky barriers and bulk Silicon in series

discussed in section 1.3. The transport equation governing thermal and electrical currents in materials i=1,2 is given by:

$$\begin{pmatrix} \vec{J}_i \\ \vec{Q}_i \end{pmatrix} = \begin{pmatrix} L_{11} & L_{12} \\ L_{21} & L_{22} \end{pmatrix}_i \begin{pmatrix} \nabla V_i \\ -\nabla T_i \end{pmatrix} \tag{6.2}$$

We solve for the thermopower, S, across the entire device by requiring $\vec{J}$ and $\vec{Q}$ to be continuous, and by relating the voltage drops across the sample via $x_{SB}\nabla V_{SB} + x_b\nabla V_b = L\nabla V$, where L is the total length of the device. If the thermal conductivity,

κ, is the same for both the Schottky barrier and bulk sections of the SiNW, then after a bit of algebra we arrive at the following simple relation:

$$S = \frac{x_{SB}S_{SB} + x_b S_b}{x_{SB} + x_b} \tag{6.3}$$

which simply states that the thermopower across the device is the sum of the thermopower for each piece, weighted by it's length. This makes sense classically, as the temperature difference across each piece is just a fraction of ΔT determined by the length, and the fact that we can simply add voltages in series.

We now model the thermopower in each region. We begin with the "bulk" SiNW region. Thermopower in bulk Si was previously studied in n-doped samples of donor concentrations ranging from 4×10^{13} to $6 \times 10^{19}\text{cm}^{-3}$ [85]. Low doped samples were found to exhibit a "hump" in TEP at low temperatures due to phonon drag, yet the heavily doped samples appear to have a linear temperature dependence, similar to the metallic TEP response [85, 86]. The samples we received from Harvard were grown using high Boron:Silane gas flow rates and it is reasonable to expect them to be heavily doped.

With this in mind, we calculate the TEP for a degenerately doped semi-conductor using a simple parabolic band model:

$$E_F = \hbar^2 k_F^2/2m^* \qquad E_F = \frac{(3\pi^2)^{2/3}\hbar^2}{2m^*} n^{2/3} \tag{6.4}$$

where n is the electron density and m^* is the effective mass. From the Drude model, the energy dependent conductivity can be expressed $\sigma(E) = n(E)e^2\tau/m^*$, where we take the scattering time, τ, to be energy independent. We now solve the Mott formula within this framework and we arrive at the following expression relating TEP to the density:

$$S = \frac{\pi^2 k_B^2 m^*}{(3\pi^2)^{2/3}\hbar^2 e} \frac{T}{n^{2/3}} \tag{6.5}$$

When the device is strongly turned on ($V_g \ll V_{th}$), the Schottky barrier is presumed to be extremely thin. We consider the simple case when the Schottky barrier

width is negligible compared with the total length of the device, and extract the charge density from the behavior of the saturated TEP (figure 6.7) using equation 6.5. Using for the effective mass $m^* \sim 0.39m_e$ [83], we calculate the density to be $n \sim 1.4 \times 10^{19}\text{cm}^{-}3$. For degenerately doped Si, all the charge carriers come from ionized dopantsl We therefore estimate $n_B \sim 1.4 \times 10^{19}\text{cm}^{-}3$. Although the doping concentration for the Harvard produced SiNW's is not known, this is a reasonable value. The wires were grown with a 5000:1 Si:B gas flow rate corresponding to a doping of $5.3 \times 10^{20}\text{cm}^{-3}$ at full converstion, but we do not expect all of the Boron to be converted.

Now we turn our attention to the Schottky barrier piece. When the SiNW device begins to turn off ($C_g \sim V_{th}$) and the Schottky barrier becomes wide, we expect conduction in the SiNW to be dominated by thermal activation over the barrier. Just as in the case of the semi-conducting SWNT, we expect a constant $S_{SB} \sim 300\mu\text{V/K}$ contribution to the TEP, independent of temperature. Unlike the s-SWNT, however, the peak in S of the SiNW decreases as T decreases as shown in figure 6.5. This peak lowering behavior can be explained considering a simple model of the SB and bulk-Si in series, as follows. It is reasonable to expect the Schottky barrier region and the bulk region to both contribute to the overall TEP. Near device turnoff ($V_g \sim V_{th}$), as the temperature is lowered the TEP contribution from the bulk becomes less. Due to the weighting from the bulk piece (equation 6.3) we expect that the maximum in SiNW TEP decreases with temperature, unlike the case of the CNT where it remains constant. We do observe this peak lowering, suggesting that our simple model of SB and bulk-Si in series can qualitatively explain our measurement results.

These thermoelectric measurements are promising in the SiNW because they can help shed light on the transport mechanism in the wire. In addition, for the case of degenerately doped wires, they might also provide a reasonable independent estimate for the dopant density. In conjunction with conductance measurements the TEP measurement can be a powerful tool. The TEP measurements performed here investigated devices with quite low mobilities. It should prove interesting to

measure TEP in high performance SiNW devices in the future.

7 Conclusions

We have performed gate and temperature dependent TEP and G measurements on a variety of 1d systems and transport regimes. We were able to verify the validity of the mesoscopic Mott formula in SWNTs, as we found excellent quantitative agreement between the predicted and measured TEP in m-SWNTs. As these systems were cooled were able to make a quantitative measurement of the TEP oscillations in the Coulomb blockade regime, owing to the unique design of our mesoscale thermoelectric device. The amplitude and shape of the sawtooth oscillations agree well with the theory.

TEP in the s-SWNT was found to be large and highly variable under gate electric field modulation. A simple Schottky barrier model governing electrical transport in the s-SWNT produced values in good agreement with our measurement. From the data we were able to extract a very reasonable value of $\Delta \sim 160$meV for the Schottky barrier height for a typical p-type s-SWNT.

The MWNT was also found to obey the Mott formula within the framework of a multi-channel parallel conduction model. Contributions of TEP from the individual shells were observed to weight with their corresponding conductance. From the TEP data we were able to extract the density of states in the MWNT as a function of the temperature. With a geometric estimate of the capacitive gate coupling we extracted the number of single sub-band current carrying shells in the MWNT, N_{eff}. We found a reasonable number of 5-10 active shells at room temperature, cooling to roughly 1 shell at low temperature. Further investigation into $N_{eff}(T)$ may provide information about the intershell interaction energy in the MWNT.

Finally, measurements in the SiNW exhibited TEP similar to that of the SB controlled s-SWNT, but with a weighted contribution to the TEP from bulk Si based on the relative widths of the SB and the bulk nanowire regions. These findings agree qualitatively with a simple model of series transport through a SB and bulk SiNW.

References

[1] R. Saito, G. Dresselhaus, and M. S. Dresselhaus, *Physical Properties of Carbon Nanotubes* (Imperial College Press, London, 1998).

[2] W. Liang, M. Bockrath, and H. Park, Phys. Rev. Lett. **88**, 126801 (2002).

[3] A. A. M. Staring *et al.*, Europhys. Lett. **22**, 57 (1993).

[4] A. Urbina *et al.*, Phys. Rev. Lett. **90**, 106603 (2003).

[5] A. Bachtold *et al.*, Nature **397**, 673 (1999).

[6] B. Bourlon *et al.*, Phys. Rev. Lett. **93**, 176806 (2004).

[7] P. G. Collins, M. S. Arnold, and P. Avouris, Science **292**, 706 (2001).

[8] P. G. Collins and P. Avouris, Appl. Phys. A **74**, 329 (2002).

[9] Y. Cui *et al.*, Appl. Phys. Lett. **78**, 2214 (2201).

[10] J. M. Ziman, *Electrons and Phonons* (Oxford, Cambridge, 1960).

[11] L. Onsager, Phys. Rev. **37**, 405 (1931).

[12] T. S. Moss, *Handbook on Semiconductors* (Elsevier Science Publishers B. V., Amsterdam, 1992).

[13] M. Cutler and N. F. Mott, Phys. Rev. **181**, 1336 (1969).

[14] V. W. Scarola and G. D. Mahan, Phys. Rev. B **66**, 205405 (2002).

[15] J. P. Small, K. M. Perez, and P. Kim, Phys. Rev. Lett. **91**, 256801 (2003).

[16] L. D. Hicks and M. S. Dresselhaus, Phys. Rev. B **47**, 16631 (1993).

[17] R. Venkatasubramanian, E. Sivola, T. Colpitts, and B. O'Quinn, Nature **413**, 597 (2001).

[18] T. C. Harman, P. J. Taylor, M. P. Walsh, and B. E. LaForge, Science **297**, 2229 (2002).

[19] R. Venkatasubramanian et. al, *unpublished presentation*, (2003).

[20] D. Li *et al.*, Appl. Phys. Lett. **83**, 2934 (2003).

[21] B. J. van Wees *et al.*, Phys. Rev. Lett. **60**, 848 (1988).

[22] D. A. Wharam *et al.*, J. Phys. C **21**, L209 (1988).

[23] K. Schwab, E. A. Henriksen, J. M. Worlock, and M. L. Roukes, Nature **404**, 974 (2000).

[24] S. Datta, *Electronic Transport in Mesoscopic Systems* (Cambridge, United Kingdom, 1995).

[25] U. Sivan and Y. Imry, Phys. Rev. B **33**, 551 (1986).

[26] J. W. G. Wildöer *et al.*, Nature **391**, 59 (1998).

[27] T. W. Odom, J. Huang, P. Kim, and C. M. Lieber, Nature **291**, 62 (1998).

[28] M. Purewal *et al.*, to be published.

[29] T. Heinzel, *Mesoscopic Electronics in Solid State Nanostructures* (Wiley VCH, GmbH, 2003).

[30] J. Kong *et al.*, Phys. Rev. Lett. **87**, 106801 (2001).

[31] W. Liang *et al.*, Nature **411**, 665 (2001).

[32] S. J. Tans, A. R. M. Verschueren, and C. Dekker, Nature **393**, 49 (1998).

[33] R. Martel *et al.*, Appl. Phys. Lett. **73**, 2447 (1998).

[34] S. M. Sze, *Physics of Semiconductor Devices* (John Wiley and Sons, New York, 1981).

[35] R. Martel *et al.*, Phys. Rev. Lett. **87**, 256805 (2001).

[36] J. Appenzeller *et al.*, Phys. Rev. Lett. **89**, 126801 (2002).

[37] F. Léonard and J. Tersoff, Phys. Rev. Lett. **84**, 4693 (2000).

[38] S. Heinze *et al.*, Phys. Rev. Lett. **89**, 106801 (2002).

[39] S. J. Wind, J. Appenzeller, and P. Avouris, Phys. Rev. Lett. **91**, 058301 (2003).

[40] V. Derycke, R. Martel, J. Appenzeller, and P. Avouris, Appl. Phys. Lett. **80**, 2773 (2002).

[41] M. Freitag, M. Radosavljevic, Y. Zhou, and A. T. Johnson, Appl. Phys. Lett. **79**, 3326 (2001).

[42] M. Krüger, M. R. Buitelaar, T. Nussbaumer, and C. Schönenberger, Appl. Phys. Lett. **78**, 1291 (2001).

[43] A. Javey *et al.*, Nature **424**, 654 (2003).

[44] S. Rosenblatt *et al.*, Nano Lett. **2**, 869 (2002).

[45] A. Bachtold, P. Hadley, T. Nakanishi, and C. Dekker, Science **294**, 1317 (2001).

[46] C. Zhou, J. Kong, and H. Dai, Appl. Phys. Lett. **76**, 1597 (2000).

[47] A. Javey, M. Shim, and H. Dai, Appl. Phys. Lett. **80**, 1064 (2002).

[48] T. Nakanishi, A. Bachtold, and C. Dekker, Phys. Rev. B **66**, 073307 (2002).

[49] S. Heinze, M. Radosavljevic, J. Tersoff, and P. Avouris, Phys. Rev. B **68**, 235418 (2003).

[50] M. Radosavljevic, S. Heinze, J. Tersoff, and P. Avouris, Appl. Phys. Lett. **83**, 2435 (2003).

[51] Z. Chen *et al.*, Nano Lett. **5**, 1497 (2005).

[52] Y. Chen and M. S. Fuhrer, Phys. Rev. Lett. **95**, 236803 (2005).

[53] X. Zhou *et al.*, Phys. Rev. Lett. **95**, 146805 (2005).

[54] J. P. Small and P. Kim, Microscale Thermophys. Eng. **8**, 1 (2004).

[55] J. Hone *et al.*, Phys. Rev. Lett. **8-**, 1042 (1998).

[56] P. G. Collins, K. B. andM. Ishigami, and A. Zettl, Science **287**, 1801 (2000).

[57] K. Bradley *et al.*, Phys. Rev. Lett. **85**, 4361 (2000).

[58] G. U. Sumanasekera *et al.*, Phys. Rev. Lett. **89**, 166801 (2002).

[59] M. Bockrath *et al.*, Science **291**, 283 (2001).

[60] M. T. Woodside and P. L. McEuen, Science **296**, 1098 (2002).

[61] C. Zhou, J. Kong, and H. Dai, Phys. Rev. Lett. **84**, 5604 (2000).

[62] Tinkham, *Introduction to Superconductivity* (McGraw-Hill, New York, 1996).

[63] H. Grabert and M. H. Devoret, *Single Charge Tunneling* (Plenum Press, New York, 1992).

[64] M. Bockrath *et al.*, Science **275**, 1922 (1997).

[65] J. Cao, Q. Wang, and H. Dai, Nature Materials **4**, 745 (2005).

[66] U. C. Coskun *et al.*, Science **304**, 1132 (2004).

[67] B. Babic, T. Kontos, and C. Schonenberger, Phys. Rev. Lett. **70**, 235419 (2004).

[68] C. W. J. Beenakker and A. A. M. Starling, Phys. Rev. B **46**, 9667 (1992).

[69] L. W. Molenkamp *et al.*, Semicond Sci Technol **9**, 903 (1994).

[70] L. W. Molenkamp *et al.*, Phys. Rev. Lett. **65**, 1055 (1990).

[71] M. C. Llaguno, J. E. Fischer, A. T. Johnson, and J. Hone, Nano. Lett. **4**, 45 (2004).

[72] S. Frank, P. Poncharal, Z. L. Wang, and W. A. de Heer, Science **280**, 1744 (1998).

[73] P. G. Collins *et al.*, Phys. Rev. Lett. **86**, 3128 (2001).

[74] S. Bandow, S. Asaka, X. Zhao, and Y. Ando, Appl. Phys. A **67**, 23 (1998).

[75] Y. Cui, X. Duan, J. Hu, and C. M. Lieber, J. Phys. Chem. B **104**, 5213 (2000).

[76] G. Gu *et al.*, Appl. Phys. Lett. **90**, 5747 (2001).

[77] X. Duan, Y. Cui, J. Wang, and C. M. Lieber, Nature **409**, 66 (2001).

[78] Y. Wu *et al.*, Nano. Lett. **4**, 433 (2004).

[79] G. Zheng, W. Lu, S. Jin, and C. M. Lieber, Adv. Mater. **16**, 1890 (2004).

[80] Y. Cui and C. M. Lieber, Science **291**, 851 (2001).

[81] A. M. Morales and C. M. Lieber, Science **279**, 208 (1998).

[82] Y. Cui *et al.*, Nano. Lett. **3**, 149 (2003).

[83] Z. Zhong, Y. Fang, W. Lu, and C. M. Lieber, Nano. Lett. **5**, 1143 (2005).

[84] Y. Ahn, J. Dunning, and J. Park, Nano. Lett **5**, 1367 (2005).

[85] M. E. Brinson and W. Dunstan, J. Phys. C **3**, 483 (1970).

[86] T. H. Geballe and G. W. Hull, Phys. Rev. **98**, 940 (1955).

A Appendix A - SWNT growth

We use the chemical vapor deposition method (CVD) to grow our CNT's. Other methods, such as laser ablation, tend to produce nanotubes with greater amounts of defects.

B Appendix B - CNT Nanogap Fabrication